

**A ROUGHNESS CORRECTION FOR AQUARIUS OCEAN
BRIGHTNESS TEMPERATURES USING THE CONAE
MICROWAVE RADIOMETER**

by

YAZAN HENRY LUTFI HEJAZIN

B.S. in Telecommunication Engineering - Princess Sumaya University for Technology, 2010

M.S. in Electrical Engineering – University of Central Florida, 2015

A dissertation submitted in partial fulfillment of the requirements
for the degree of Doctor of Philosophy
in the Department of Electrical Engineering and Computer Science
in the College of Engineering and Computer Science
at the University of Central Florida
Orlando, Florida

Spring Term
2015

Major Professor: W. Linwood Jones

© 2015 Yazan Henry Hejazin

ABSTRACT

Aquarius/SAC-D is a joint NASA/CONAE (Argentine Space Agency) Earth Sciences satellite mission to measure global sea surface salinity (SSS), using an L-band radiometer that measures ocean brightness temperature (Tb). The application of L-band radiometry to retrieve SSS is a difficult task, and therefore, precise Tb corrections are necessary to obtain accurate measurements. One of the major error sources is the effect of ocean roughness that “warms” the ocean Tb. The Aquarius (AQ) instrument (L-band radiometer/scatterometer) baseline approach uses the radar scatterometer to provide this ocean roughness correction, through the correlation of radar backscatter with the excess ocean emissivity.

In contrast, this dissertation develops an ocean roughness correction for AQ measurements using the MicroWave Radiometer (MWR) instrument Tb measurements at Ka-band to remove the errors that are caused by ocean wind speed and direction. The new ocean emissivity radiative transfer model was tuned using one year (2012) of on-orbit combined data from the MWR and the AQ instruments that are collocated in space and time. The roughness correction in this paper is a theoretical Radiative Transfer Model (RTM) driven by numerical weather forecast model surface winds, combined with ancillary satellite data from WindSat and SSMIS, and environmental parameters from NCEP. This RTM provides an alternative approach for estimating the scatterometer-derived roughness correction, which is independent. The theoretical basis of the algorithm is described and results are compared with the AQ baseline scatterometer method. Also results are presented for a comparison of AQ SSS retrievals using both roughness corrections.

*To The People Who Have Always Believed In Me And Trusted My
Judgments, A 10-Year Journey Stops Here And Another Life –Long Journey Shall
Start, And I Would Have Never Done This Without Your Support. Your Support
Was Endless And I'm Proud Of You*

To My Family And Friends

ACKNOWLEDGMENTS

I would like to deeply thank my advisor, Prof. W. Linwood Jones, for all his hard work, dedication and support that guided me throughout the past five years towards my degree. His trust and vision paved my path towards success. I have learned a lot from him and will keep learning for many years to come.

I also would like to thank my committee members, Dr. Jeffery Piepmeier, Dr. Wasfy Mikhael, Dr. Parveen Wahid and Dr. William Junek for their guidance and advice and time.

Special thanks for the Central Florida Remote Sensing Laboratory team who never spared a moment to help and support me during the past five years.

I wish to acknowledge the financial support by NASA Headquarters Earth Science Program for support of the Aquarius Ocean Sea Surface Salinity science team.

Finally, I would like to acknowledge Remote Sensing Systems Inc. for providing the WindSat and SSMIS data.

TABLE OF CONTENTS

LIST OF FIGURES	viii
LIST OF TABLES	xiii
CHAPTER 1: INTRODUCTION	1
1.1 Research Objective.....	2
CHAPTER 2: AQUARIUS/SAC-D MISSION	4
2.1 Aquarius Instrument.....	5
2.2 Microwave Radiometer Instrument.....	7
CHAPTER 3: TUNING CFRSL OCEAN SURFACE EMISSIVITY MODEL	9
3.1 L-Band Model Tuning.....	14
3.1.1 Tuning L-Band Model For Wind Speed	14
3.1.2 Tuning L-Band Model For Wind Direction.....	17
3.2 Ka-Band Model Tuning	21
3.2.1 Tuning Ka-Band Model For Wind Speed.....	24
3.2.2 Tuning Ka-Band Model For Wind Direction	27
CHAPTER 4: AQUARIUS OCEAN ROUGHNESS CORRECTION	32
4.1 MWR Roughness Correction	32
4.1.1 AQ/MWR Forward Isotropic RTM	34
4.2 AQ Roughness Correction Algorithm.....	37

4.3 MWR-Derived Roughness Correction	38
CHAPTER 5: SEA SURFACE SALINITY	42
5.1 Salinity Retrieval Algorithm	43
5.2 Hybrid Coordinate Ocean Model (HYCOM) Salinity	47
CHAPTER 6: RESULTS AND VALIDATION	50
6.1 CFRSL Retrieved Salinity.....	50
CHAPTER 7: SUMMARY.....	56
6.1 Future Work	57
APPENDIX A SMOOTH SEA SURFACE EMISSIVITY.....	58
APPENDIX B SALINITY EFFECTS ON OCEAN EMISSIVITY	65
APPENDIX C ROUGH SEA SURFACE EMISSIVITY.....	68
APPENDIX D CENTRAL FLORIDA REMOTE SENSING LABORATORY EMISSIVITY MODEL	72
APPENDIX E RELATIVE WIND DIRECTION	77
APPENDIX F AQUARIUS SCATTEROMETER ROUGHNESS CORRECTION	84
REFERENCES	88

LIST OF FIGURES

Figure 1 Aquarius /SAC-D observatory and instruments.....	5
Figure 2 Aquarius three beam radiometer measurement geometry [8]. The arrow shows the flight direction of the spacecraft.....	6
Figure 3 Measurements geometry of the MicroWave Radiometer and Aquarius.	8
Figure 4 The tuning process for the CFRSL model.....	12
Figure 5 Bin average plots of modeled (red) and observed (blue) brightness temperature at L-band. The top three panels show results for beam 1 (left), beam 2 (middle) and beam 3 (right) for V-pol. The bottom three panels show results for beam 1 (left), beam 2 (middle) and beam 3 (right) for H-pol.	16
Figure 6 L-band β coefficients as function of wind speed. Left panel shows the Vertical polarization and right panel shows the horizontal polarization. Top panel shows β_1 and bottom panel shows β_2	17
Figure 7 L-band wind direction excess brightness temperature model comparison with Yueh 2010 [18], for beam 1.....	18
Figure 8 Modeling of the relative wind direction at L-band for four different wind speed values (6, 9, 12 and 15 m/s). The top three panels show results for beam 1 (left), beam 2 (middle) and beam 3 (right) for V-pol. The bottom three panels show results for beam 1 (left), beam 2 (middle) and beam 3 (right) for H-pol.....	19
Figure 9 Correlation between L-band total observed (blue) and modeled (red) brightness temperature for each beam and polarization for the three incidence angles of Aquarius. Results are shown for three wind speed values namely; 4, 8 and 15 m/s.....	20

Figure 10 Ascending passes coverage of the collocations between MWR, SSMIS and WindSat data over one week period.	22
Figure 11 Tuning process for Ka-band model.	23
Figure 12 Relative probability of oceanic wind speed values for the year 2013 from AQ Level-2 data.	25
Figure 13 Bin average plots of modeled (red) 36.5 GHz and observed (blue) ocean surface brightness temperature at Ka-band. The top two panels show the results for the odd (left) and even (right) beams for V-pol. The bottom two panels show results for the odd (left) and the even (right) beams for H-pol.	26
Figure 14 Ka-band β coefficients as function of wind speed for odd (blue) and even (red) beams. Top panel shows β_1 and bottom panel shows β_2 , and left panel shows the V- pol and right panel shows the H-pol.	27
Figure 15 Ka-band wind direction model comparison for excess brightness temperature with Wentz 1992 [22], for odd beams.	28
Figure 16 Modeling of the relative wind direction at Ka-band for four different wind speed values (6, 9, 12 and 15 m/s). The top two panels show results for odd beams (left) and even beams (right) for V-pol. The bottom two panels show corresponding results for odd beams (left) and even beams (right) for H-pol.	29
Figure 17 Correlation between the Ka-band total observed (blue) and modeled (red) ocean brightness temperature for each polarization and incidence angle of the MWR channels at two different wind speeds (6 and 10 m/s). Panel A: shows the V-pol for the odd beams; B: shows the	

H-pol for the odd beams; C: shows the corresponding V-pol for the even beams; and D: shows the H-pol for the even beams.....	30
Figure 18 Block diagram of the process of generating a cross-correlation between isotropic roughness at Ka-band and at L-band.	31
Figure 19 MicroWave Radiometer and Aquarius swath collocation. MWR 8 beams (blue dots) share the same swath with the three Aquarius beams; inner (red), middle (green) and outer (magenta).	33
Figure 20 Google Earth image of Aquarius and MicroWave Radiometer beams, showing the difference in azimuth angle, which corresponds to difference in the relative wind direction angle.	34
Figure 21 Forward models between the roughness correction at Ka-band and L-band by AQ beam#. Left panels represent the vertical polarization and right panels represent the horizontal polarization.	36
Figure 22 The process of calculating the MWR roughness correction.....	38
Figure 23 Aquarius scatterometer derived roughness (blue) and MWR derived roughness (red). Left panels represent the vertical polarization and right panels represent the horizontal polarization. First row represents Aquarius beam 1, second row represents Aquarius beam 2 and the third row represents Aquarius beam 3.....	39
Figure 24 Flow chart of the roughness correction process	41
Figure 25 Brightness temperature as a function of sea surface temperature at different constant salinity.....	42
Figure 26 Signal received by Aquarius [19].	46

Figure 27 HYCOM In-Situ data sources.	48
Figure 28 Six hours average of HYCOM salinity on January 2 nd , 2014 [31].....	49
Figure 29 Difference between AQ salinity and HYCOM (blue) and MWR salinity and HYCOM (red). First row represents Aquarius beam 1, second row represents Aquarius beam 2 and the third row represents Aquarius beam 3.....	51
Figure 30 Global delta sea surface salinity derived using scatterometer roughness correction. ..	53
Figure 31 Global delta sea surface salinity derived using MWR roughness correction.	53
Figure 32 Histograms of global salinity differences.....	54
Figure 33 Salinity double differences. Top panel shows the relation between wind speed and the double differences and the bottom panel shows the relation between the relative wind direction and the double differences.	55
Figure 34 Plane wave electric field reflection and transmission at water-air boundary [10].	60
Figure 35 The real part (left panel) and imaginary part (right panel) of the dielectric constant for salinity values of 0, 25, 30, 35 and 40 psu at sea surface temperature of 25 C°.....	62
Figure 36 Power reflection coefficient for vertical and horizontal polarizations at constant sea surface temperature (25 C°), salinity (34 psu), at the AQ frequency (1.413 GHz).	63
Figure 37 Microwave radiative transfer block-diagram over ocean.	64
Figure 38 Smooth sea surface emissivity at 1.413 GHz for 25 C° SST, and 10 and 30 psu salinity.	67
Figure 39 Foam fraction as a function of wind speed.....	75
Figure 40 Oceanography and meteorology convention for wind direction measurements	78
Figure 41 Azimuth angle measurement.	80

Figure 42 Azimuth angles of the 8 MWR forward looking beams for one orbit.....	80
Figure 43 Relative wind direction measurement [44].....	81
Figure 44 The relationship between the scatterometer vertical backscatter (in dB) and the vertical ocean roughness (in Kelvin).	86
Figure 45 The relationship between the significant wave height (in meters) and the vertical ocean roughness (in Kelvin).....	86

LIST OF TABLES

Table 1 Coefficients of wind speed effect model for L-band.	15
Table 2 Root mean square error between measured and modeled brightness temperature at L-band for different ranges of wind speed.	16
Table 3 Coefficients of wind speed effect model for Ka-band.	25
Table 4 Root mean square error between measured and modeled brightness temperature at Ka-band for different ranges of wind speed.	26
Table 5 Coefficients of the conversion formula from Ka-band roughness to L-band roughness.	37
Table 6 Aquarius salinity retrieval error table [2].	44
Table 7 Mean and standard deviation of the difference between MWR derived salinity and HYCOM salinity at different ranges of wind speed.	52
Table 8 Coefficients of wind speed effect model.	76
Table 9 The coefficients of the 8 th order polynomial for the first and the second harmonics of the wind direction effects for all frequency, polarization and incidence angle values.	83

CHAPTER 1: INTRODUCTION

Measuring the global sea surface salinity (SSS) is the major scientific goal of NASA's Aquarius satellite mission, which indirectly provides scientists with information about the Earth's hydrological cycle. Thus, SSS can be used as a tracer that indicates how the natural reciprocation of fresh water (precipitation and evaporation) occurs between oceans and atmosphere, and by monitoring these global changes in SSS, scientist can understand how the global hydrological cycle over the oceans influences weather and climate.

Passive microwave remote sensing plays a significant role in providing oceanic and atmospheric environmental parameter measurements with high degree of accuracy and at a global scale. Using satellite remote sensors enables scientist to acquire more data, much faster, and uniformly samples on a global scale than is possible with in-situ techniques.

Field testing, using airborne passive microwave sensors, has demonstrated that changes in SSS can be inferred by radiometric measurements of small changes the electromagnetic emission of seawater, when operating at a low frequency (long wavelength) [1]. Based upon this, the Aquarius/SAC-D mission was developed to monitor the seasonal and annual changes in ocean salinity with a high level of accuracy by providing weekly global maps of with a spatial resolution of 150 km.

Achieving accurate global SSS measurements from a satellite is a very challenging task because there are many brightness temperature (T_b) corrections that need to be made to remove unwanted T_b sources, which include: cosmic noise from the galaxy, solar emissions, mixing of polarized ocean emissions when propagating through the ionosphere and ocean surface warming

due to wave and wind roughness. After providing correction for these effects, the greatest source of uncorrected Tb error is associated with the ocean wind speed roughness effect that produces an additive excess brightness temperature [2]. Because of the transient nature of the ocean winds, correction cannot be determined a priori, and only simultaneous measurements averaged over the AQ antenna footprints on the ocean surface will suffice.

Therefore, in addition to the NASA provided AQ L-Band radiometer/scatterometer, the Argentine Space Agency CONAE (Comisión Nacional de Actividades Espaciales) has provided another passive microwave sensor (the MicroWave Radiometer, MWR) to make Tb measurements at K- and Ka-Band, which provide Nyquist spatial sampling over the AQ measurements swath and which can be used to correct the AQ ocean surface Tb's for the effects of ocean roughness and precipitation (rainfall).

1.1 Research Objective

The objective of this dissertation is to use coincident Tb measurements from the CONAE MWR onboard the Aquarius/SAC-D satellite to correct for the ocean surface roughness effect and thereby improve the AQ SSS measurements.

This objective is subdivided into three major research tasks:

1. Development of an empirical electromagnetic (EM) radiative transfer model (RTM) effort to characterize the rough ocean surface emissivity at the AQ L-Band and MWR Ka-Band frequencies, polarizations and earth viewing angles.

2. Given this RTM, develop a practical signal processing algorithm to process the satellite data stream of AQ and MWR Tb's and ancillary numerical weather model data to yield simultaneous, collocated excess Tb roughness correction for AQ.
3. To conduct a comprehensive validation effort to verify that the MWR roughness correction is effective under the majority of ocean observing conditions and to quantify this improvement in the AQ SSS measurements.

Following this introductory chapter, the organization of this dissertation is as follows. Chapter 2 describes the Aquarius/SAC-D mission science objective and discusses pertinent details of the two microwave radiometer instruments (AQ and MWR) on board the spacecraft. In Chapter 3, the statistical procedure for tuning the Central Florida Remote Sensing Laboratory RTM is described and the resulting RTM coefficients for rough ocean emissivity are presented. Next, Chapter 4 describes the derivation of the MWR algorithm for estimating the ocean surface roughness correction, and the description of the AQ project sea surface salinity (SSS) retrieval algorithm is presented in Chapter 5. Chapter 6 presents the validation results for the MWR roughness correction, which includes its impact on the retrieved SSS. Finally, Chapter 7 presents the dissertation conclusion and recommendations for future work.

CHAPTER 2: AQUARIUS/SAC-D MISSION

Salinity defined as the concentration of dissolved salt in water, is an important geophysical parameter in the study of the Earth's climate change. Global salinity measurements from space can help geophysicists to observe two major components of the earth's climate system, namely: hydrologic (water) cycle and ocean circulation [2].

Earth is an "Ocean Planet"; therefore the ocean is the dominant player in the Earth's water cycle between ocean, atmosphere, and land, and by monitoring the spatial and temporal variations in salinity, the ocean's eminent role in the Earth's water cycle can be better understood. By measuring salinity changes caused by evaporation, ice melting, precipitation (rain and snow), and rivers runoff, scientists can gather information of how the water transfers around the Earth [3].

Aquarius/SAC-D is an earth observation satellite science mission, with the objective to provide global and long-term salinity measurements. This mission is a partnership between NASA and CONAE. The satellite was launched on June 10, 2011 from Vandenberg Air Force Base in California, and it flies in a sun-synchronous polar orbit with an altitude of 657 kilometers and an inclination of 98.6° . The orbit has an exact repeat every 103 orbits (~7 days), which meets the mission requirements of generating salinity maps of the entire ocean once a week, at a resolution of 150 kilometers [4].

For the salinity measurements, the two remote sensors involved are Aquarius (AQ) and the MicroWave Radiometer (MWR); these instruments are mounted on the Argentina-built spacecraft, Satélite de Aplicaciones Científicas (SAC-D) [5] as shown in Figure 1. Aquarius, the prime mission instrument, is a microwave L-band passive/active (radiometer/scatterometer) instrument

that was developed jointly by NASA, Goddard Space Flight Center and the Jet Propulsion Laboratory. Also, there are several CONAE supplied instruments, but for this dissertation only the MWR is germane. This 3-channel passive microwave instrument supports AQ science objective and provides collocated geophysical measurements (oceanic wind speed, rain rate, and sea ice), which are useful in the salinity retrieval.

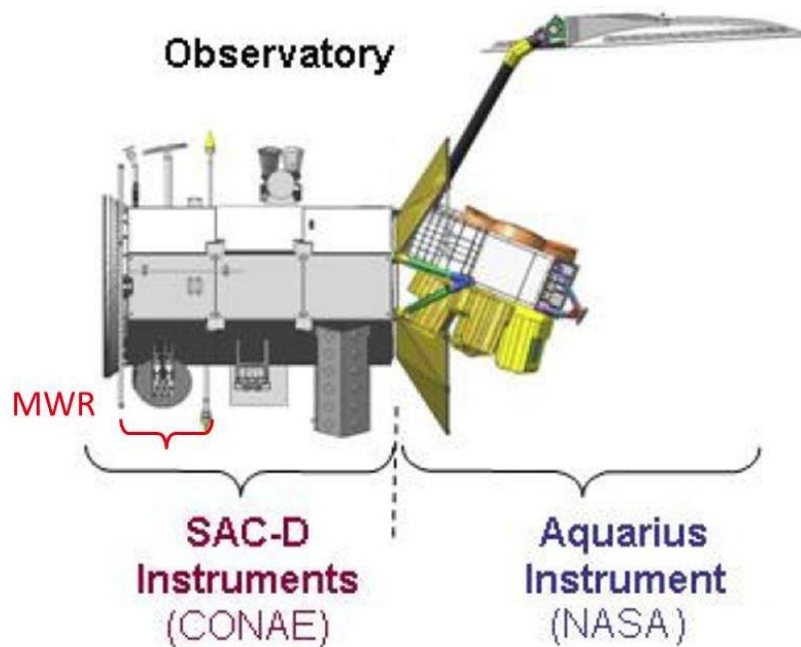


Figure 1 Aquarius /SAC-D observatory and instruments.

2.1 Aquarius Instrument

The Aquarius is an active/passive microwave remote sensor, which simultaneously measures ocean emitted brightness temperature (T_b) and radar backscatter at L-band [6]. The antenna system uses a 2.5 m offset parabolic reflector producing three spot-beams to obtain measurements in a push-broom fashion, as shown in Figure 2. These beams are formed by separate

dual linear polarized (vertical, V-pol, and horizontal, H-pol) feed horns that are pointed roughly perpendicular to the flight direction. The three beams point at incidence angles 29.3° , 38.4° and 46.3° for the inner, middle and outer beams respectively, which create three instantaneous fields of view (IFOV's) at the intersection with the Earth's surface with a resolution of 79×94 km for the inner beam, 84×120 km for the middle beam, and 96×156 km for the outer beam, resulting in a swath of approximately 390 km [7]. Since AQ/SAC-D flies in a sun-synchronous terminator earth orbit, all beams view the earth surface on the night side (away from the sun, to avoid solar contamination).

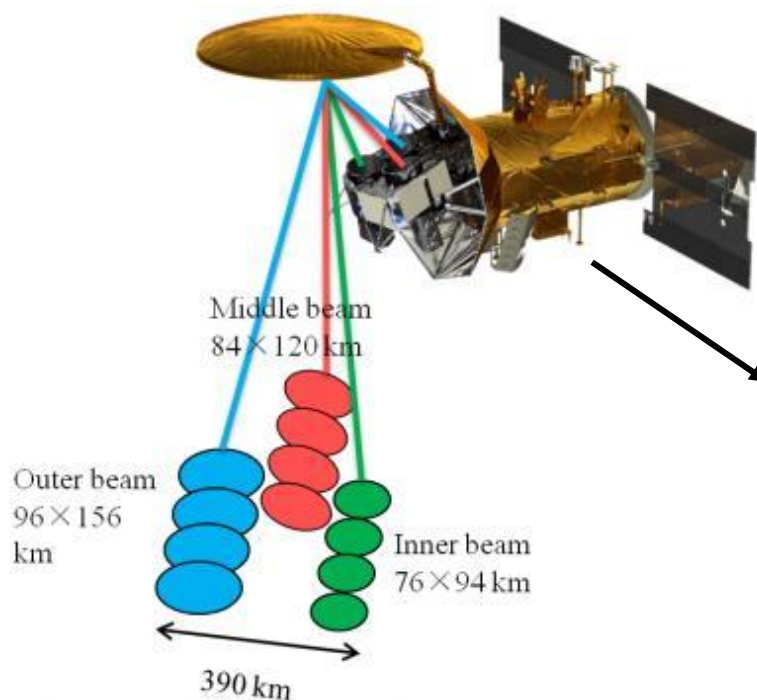


Figure 2 Aquarius three beam radiometer measurement geometry [8]. The arrow shows the flight direction of the spacecraft

The AQ comprises both passive and active portions of the instrument. The passive microwave radiometer operates at 1.4 GHz, with two Dicke receivers per feed to capture the linearly polarized (horizontal and vertical) ocean Tb's. The active part is a single scatterometer (radar) that operates at 1.26 GHz and is multiplexed (time shared between the feeds and polarizations) to capture the ocean normalized radar cross section (σ_0). The principal purpose of the scatterometer is to measure the ocean roughness backscatter from which surface wind speed and a radiometric sea surface roughness correction is derived.

2.2 Microwave Radiometer Instrument

MWR consists of three separate radiometer receivers, one operating at 23.8 GHz (K-band) H-pol, and two operating at 36.5 GHz (Ka-band) H- & V-pol. The MWR measurement geometry is similar to AQ in that it also images the surface in a push-broom fashion and covers the same swath, as shown in Figure 3. However for MWR, there are two off-set parabolic reflector antennas (forward looking and aft looking) producing 8 footprints on the ground, arranged in two conical arcs. The closest arc, to the sub-satellite point, contains the odd beams with Earth Incidence Angle (EIA~52°), and the farthest arc contains the even beams (EIA~58°). Each MWR receiver is time multiplexed using an electronic antenna switch matrix to sequentially connect to a set of eight feed-horns. The 8 forward looking beams are 36.5 GHz dual polarized and are connected to two separate receivers. On the other hand, the 8 afterward looking beams are connected to a single 23.8 GHz H-pol channel receiver.

These two sets of MWR beams provide better than Nyquist spatial sampling of the three AQ beams over the measurement swath. A special provision of yaw steering of the SAC-D

spacecraft compensates for the rotation of the earth and yields excellent collocation of the forward and aft beams over the AQ footprints [9]. Also, the collocated MWR measurements are displaced \pm several minutes from the AQ observations. However, given the MWR spatial resolution of ~ 50 km, these time differences are negligible and the collocated AQ/MWR observations are effectively simultaneous.

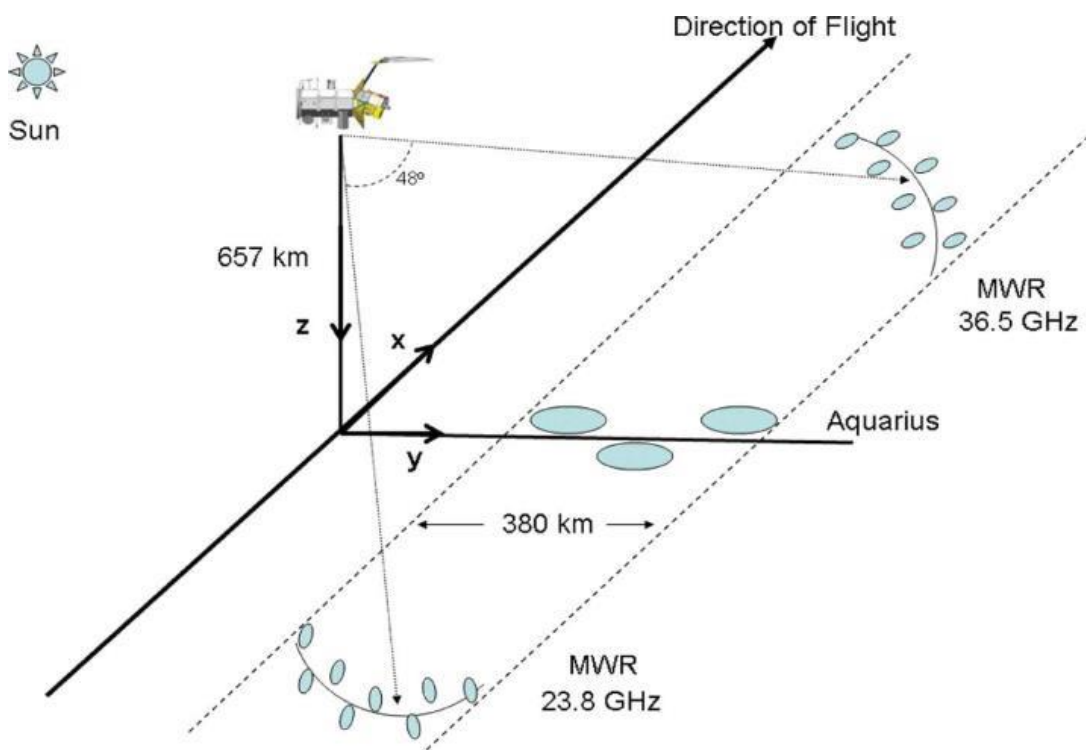


Figure 3 Measurements geometry of the MicroWave Radiometer and Aquarius.

CHAPTER 3: TUNING CFRSL OCEAN SURFACE EMISSIVITY MODEL

It is assumed that the reader is familiar with microwave radiometry and radiative transfer theory and ocean surface emissivity concepts; however, for completeness, a series of tutorials are presented in *Appendix A* through *E*. Specifically, in *Appendix A*, a tutorial on ocean Fresnel voltage reflection coefficients and the associated specular (smooth surface) emissivity is presented. In *Appendix B*, a discussion is given of the effect of a variable sea surface salinity on the specular ocean surface emissivity. The next *Appendix C* presents the concept of rough ocean emissivity caused by surface winds and waves and the associated excess ocean T_b is described. The previous development of the CFRSL ocean surface emissivity model (hereafter called the *CFRSL model*) is summarized in *Appendix D*, and finally, the concept of relative wind direction is defined in *Appendix E*.

As discussed in Chapter 1, the stated objective of this dissertation is “to use the collocated MWR measured brightness temperatures at Ka-band to develop an *ocean roughness correction* for the AQ sea surface salinity retrieval.” This roughness correction is required to remove the excess T_b that is caused by ocean wind vector (speed and direction) to produce the smooth surface specular brightness temperature from which the SSS is retrieved.

To accomplish this, it was elected to develop a theoretical ocean surface emissivity model that accurately describes the observed L-band and Ka-band rough ocean excess T_b . In the previous dissertation of El-Nimri.[10], such a model was developed for C-band; however it did not have the fidelity required for this application. Never-the-less the basis of his model was a physical ocean emissivity model by Stogryn [11] that calculates rough ocean emissivity as a function of frequency,

EIA and ocean surface wind speed (WS). By empirically tuning the model coefficients using collocated AQ and MWR Tb's with associated surface truth (WS, SST and SSS), it was possible to use this model for this application. This chapter describes the tuning process and the resulting comparison between theory and measurements over a variety of environmental conditions.

In 1967, Stogryn [11] used previous studies ([12]) to model the incremental increase in emissivity as an additive term, thus making the sea surface emissivity (ϵ_{ocean}) a summation of the specular emissivity (ϵ_{smooth}) based upon the Fresnel power reflection coefficient (*Appendix A*) and the rough surface emissivity (ϵ_{rough}),

$$\epsilon_{ocean} = \epsilon_{smooth}(freq, SST, SSS, \theta, POL) + \epsilon_{rough}(freq, WS, \chi, \theta, POL) \quad (1)$$

where $freq$ is the operating frequency, POL is the polarization of the electromagnetic (EM) blackbody emission (Vertical or Horizontal), θ is the earth incidence angle (EIA), WS is the wind speed (m/s), and χ is the relative wind direction (deg) (*Appendix E*).

The two major changes in the existing CFRSL model were to update the sea water dielectric constant model to be the AQ baseline model of Meissner and Wentz [13], which has been refined to match the observed AQ radiometer Tb measurements dependence on SSS, and the modeling of the wind direction effect. Other than this, only the empirical model coefficients were adjusted to match the observed rough surface Tb's of AQ and MWR. Because the ocean Tb's depended strongly on the ocean surface wind speed and weakly on the wind direction, it was decided to separate these two effects into an isotropic wind speed effect and an anisotropic wind direction effect. This is justified because the wind direction model is a zero mean quantity when averaged

over all relative wind directions; therefore, this decoupling greatly simplified the tuning procedure that follows.

To tune the CFRSL model for excess Tb for wind speed and wind direction, the modeled specular emissivity is calculated given SST, SSS, frequency, polarization and EIA, then it is subtracted from the measured ocean Tb, yielding the measured excess Tb ($\Delta T_{b_{meas}}$). Using the CFRSL model, the modeled excess Tb ($\Delta T_{b_{model}}$) is calculated as a function of WS and WD at each polarization and EIA for each frequency band, then the root-mean-square error between the modeled and the measured ΔT_b is calculated as,

$$RMS = \sqrt{\frac{\sum_{i=1}^n (\hat{y}_i - y_i)^2}{n}} \quad (2)$$

where n is the total number of points, i represents the ith observation (i ranges from 1 to n), \hat{y} is the estimated (CFRSL model) value and y is the observed value (AQ measured).

Figure 4 shows the flow chart of the tuning process that was applied to both AQ and MWR data.

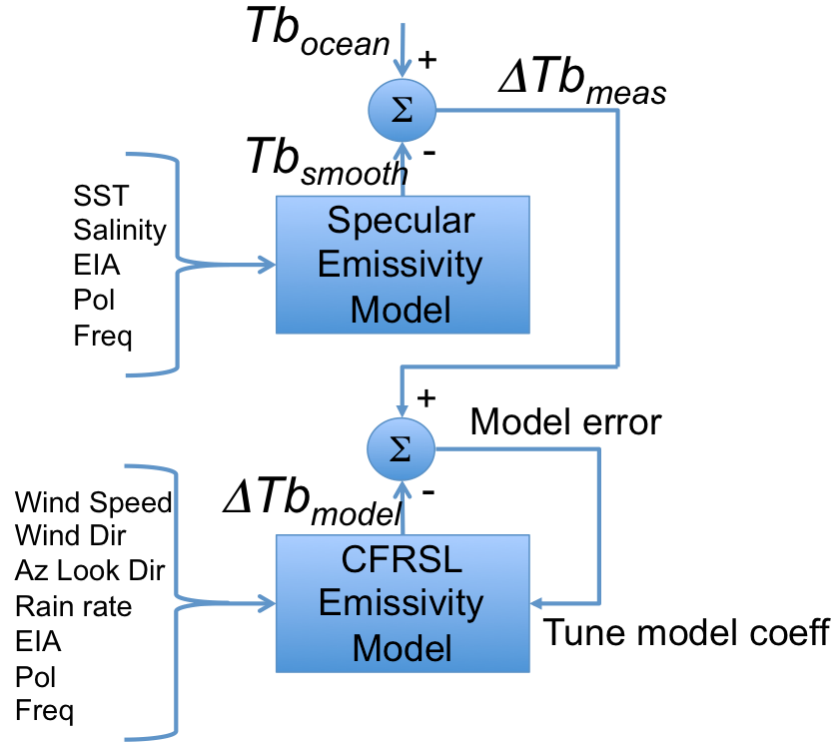


Figure 4 The tuning process for the CFRSL model.

The first step is to determine the coefficients of the wind direction and wind speed parts of the model (*Appendix C and D*).

The polarization-dependent, anisotropic wind direction effect on surface emissivity is expressed as a 2-term cosine Fourier series of the relative wind direction χ ,

$$\epsilon_{rough_{WD}} = \beta_1(WS, \theta, freq, POL) \times \cos(\chi) + \beta_2(WS, \theta, freq, POL) \times \cos(2\chi) \quad (3)$$

where the Fourier “beta” coefficients are found for fixed parameters (*freq*, *EIA* and *POL*) as a function of *WS* (*Appendix D*).

The polarization-dependent, isotropic wind speed effect for H-pol is,

$$\epsilon_{rough_{WS}}(EIA, WS, freq, SST) = (a_1 \times Z_{EIA} + a_2 \times Z_{WS} + a_3 \times Z_{EIA} \times Z_{WS}) \frac{\sqrt[4]{freq}}{SST} \quad (4)$$

where $Z_{EIA} = 0.5 + \tan^{-1}((EIA - b_1)/b_2)/\pi$, and $Z_{WS} = 0.5 + (\tan^{-1}((WS - c_1)/c_2))/\pi$.

And the corresponding V-pol wind speed effect is,

$$\epsilon_{rough_{WS}}(EIA, WS, freq, SST) = (a_0 + a_1 \times Z_{EIA} + a_2 \times Z_{WS} + a_3 \times Z_{EIA} \times Z_{WS}) \frac{\sqrt[4]{freq}}{SST} \quad (5)$$

where $Z_{EIA} = \exp(-1 \times \exp((EIA - b_1)/b_2))$, and $Z_{WS} = \exp(-1 \times \exp((WS - c_1)/c_2))$.

The isotropic surface brightness (averaged over all relative wind directions) is,

$$\langle T_{surf} \rangle_{all\ WD} = SST \times \epsilon_{rough_{WS}} + SST \times \epsilon_{smooth} \quad (6)$$

Given the surface truth SSS and SST, the specular “smooth surface” brightness is precisely known; thus, for each frequency, polarization and EIA, the coefficients for the CFRSL model were found by running an iterative loop that varies the values of the coefficients systematically until an optimum value is found that minimizes the (RMS) error between the modeled and measured (observed) surface brightness as shown in Equation (2). It is worth mentioning that the coefficients typically converge to a constant value after six iterations.

3.1 L-Band Model Tuning

For tuning the CFRSL model at L-band, the most recent Aquarius L-2 Version 3 (V3.0) data are used to match observed AQ ocean surface brightness temperature ($T_{b_{ocean}}$). The data set that is provided by the AQ science team, comprises AQ instantaneous brightness temperature measurements, the scatterometer-derived surface wind speeds, ancillary Reynold SST, and ancillary wind vector from the National Center of Environmental Predictions (NCEP), plus the collocated SSS values from the Hybrid Coordinate Ocean Model (which will be discussed later in Chapter 5) [14, 15]. All the ancillary data were resampled to the geolocation of the AQ samples on the surface.

Observed brightness temperatures from 2012 and 2013 were used for tuning and validation respectively. In each year a total of ~23,000,000 valid observation points exist (over 7,000,000 observations per beam).

3.1.1 Tuning L-Band Model For Wind Speed

For tuning the wind speed model dependence, a non-linear fit was applied to estimate the coefficients of Equations (4) and (5) to reduce the RMS error between the observed samples and the calculated samples. This process was repeated in an iterative loop, until the predicted coefficients produced an output with a maximum *RMS* error equal or lower than a chosen value of 0.4 K, since this RMS value corresponds to the total budget error allowed to achieve the SSS accuracy required by the AQ science team. The CFRSL model coefficients are shown in Table 1.

Table 1 Coefficients of wind speed effect model for L-band.

V-Pol						H-Pol					
Coef	Value	Coef	Value	Coef	Value	Coef	Value	Coef	Value	Coef	Value
a ₀	0.426	b ₁	46.375	c ₁	13.572	--		b ₁	90.684	c ₁	-48.945
a ₁	-0.005	b ₂	4.188	c ₂	11.176	a ₁	--673.2	b ₂	13.773	c ₂	53.490
a ₂	6.070	--	--	--	--	a ₂	-1.013	--	--	--	--
a ₃	-0.723	--	--	--	--	a ₃	942.63	--	--	--	--

A comparison of the six observed AQ surface Tb's (three EIA's and two polarizations) with the tuned CFRSL model are shown in Figure 5, as a function of scatterometer derived wind speed [16, 17], bin-averaged every 2 m/s. It appears that for more than 99% of ocean wind speeds (WS < 20 m/s), the modeled Tb (in red) matches in the mean of the observed Tb (in blue). For wind speeds greater than 20 m/s the two datasets diverge due to improper tuning caused by the reduced number of observations. The mean value of the curves, represented by the square symbol along the line, are a function of wind speed at a given frequency, polarization and EIA, and the standard deviation bars represent the change of Tb as a function of relative wind direction at a given wind speed value.

Table 2 shows the RMS error between the modeled and measured Tb for each of the AQ beams, at different ranges of wind speeds. The RMS error is less than the total error budget for each beam, polarization and wind speed range, and more importantly most of the RMS error is associated with the wind direction effect, which is removed during the excess roughness correction algorithm discussed in Chapter 4.

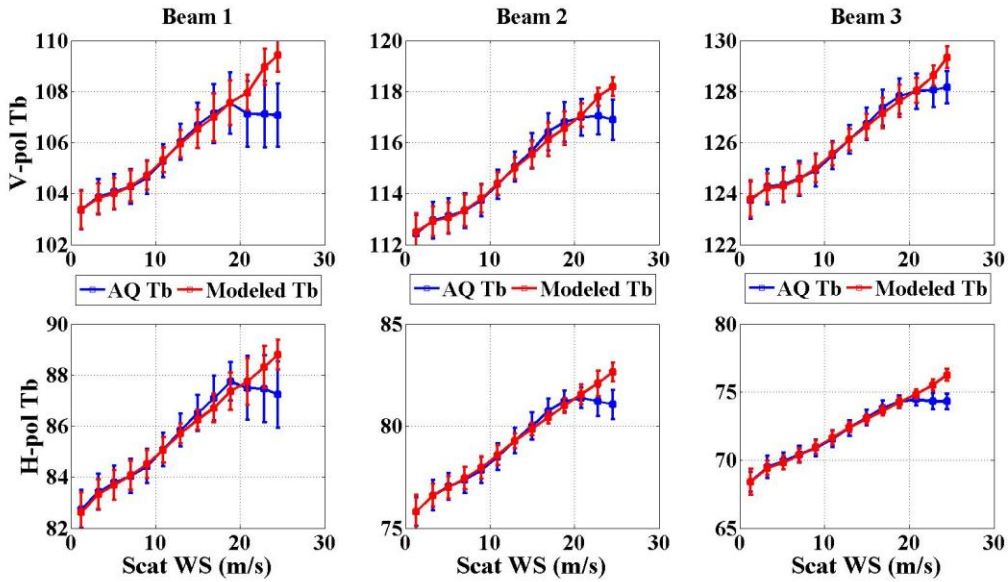


Figure 5 Bin average plots of modeled (red) and observed (blue) brightness temperature at L-band. The top three panels show results for beam 1 (left), beam 2 (middle) and beam 3 (right) for V-pol. The bottom three panels show results for beam 1 (left), beam 2 (middle) and beam 3 (right) for H-pol.

Table 2 Root mean square error between measured and modeled brightness temperature at L-band for different ranges of wind speed.

Beam Number	RMS Error in Kelvin							
	0-5 m/s		5-10 m/s		10-15 m/s		15-20 m/s	
	V-pol	H-pol	V-pol	H-pol	V-pol	H-pol	V-pol	H-pol
1	0.168	0.181	0.241	0.252	0.177	0.219	0.120	0.150
2	0.181	0.201	0.243	0.243	0.158	0.191	0.098	0.113
3	0.180	0.241	0.253	0.255	0.153	0.181	0.084	0.092

3.1.2 Tuning L-Band Model For Wind Direction

Using the same iterative technique, the coefficients of Equation (3) (β_1 and β_2) were estimated, to model the relative wind direction effect as a function of wind speed for the three AQ EIA's (29.3°, 38.4° and 46.3°). Figure 6 illustrates the changes in the β coefficients (as a function of wind speed), for each of the AQ beams and both polarizations and corresponding equations are presented in *Appendix E*. As shown in this figure, the effect of wind direction becomes larger as wind speed increases, expanding by that standard deviation of the brightness temperature at higher wind speeds, which is consistent with other AQ investigations, e.g., Yueh [18].

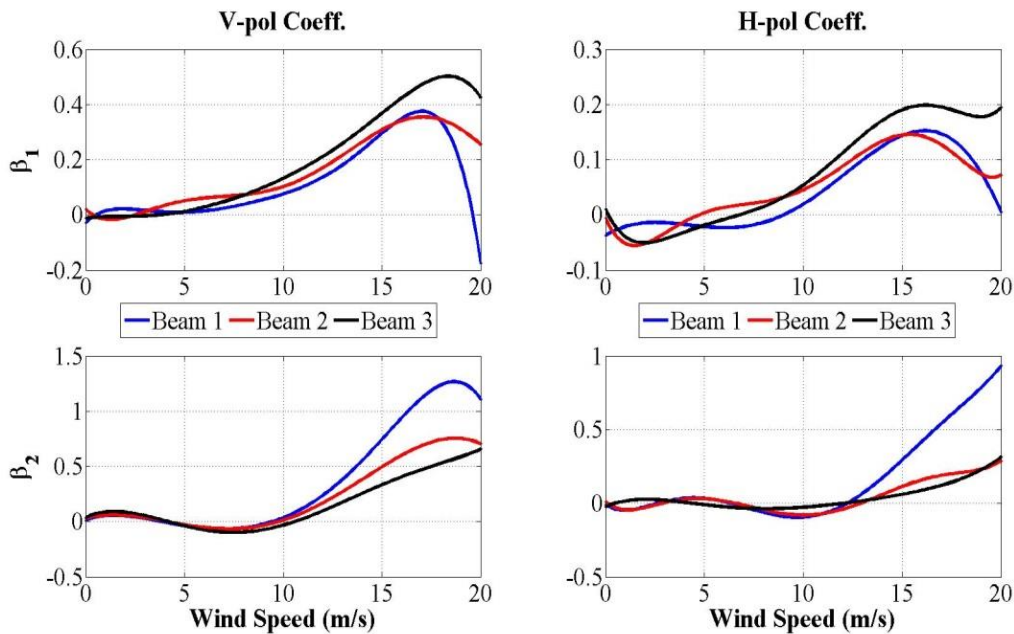


Figure 6 L-band β coefficients as function of wind speed. Left panel shows the Vertical polarization and right panel shows the horizontal polarization. Top panel shows β_1 and bottom panel shows β_2 .

Yueh [18] developed a model for the relative wind direction using data collected from the L-band active/passive sensor during a flight over Goose bay in Canada. The sensor had an EIA

close to 30° (close to EIA of AQ beam 1). Comparisons with Yueh's model are shown in Figure 7, for wind speeds values of 6 and 10 m/s. It can be observed from the figure that there is a high level of similarity between both models for both polarizations. Also, as shown in the figure, the effect of relative wind direction will increase the standard deviation of the excess Tb (ΔT_b) by ~ 1 K at higher wind speeds.

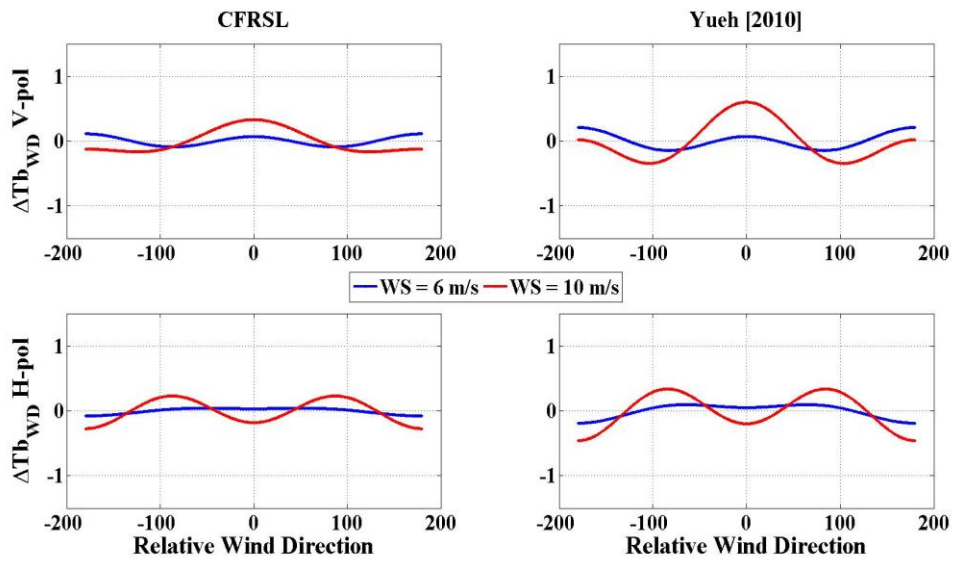


Figure 7 L-band wind direction excess brightness temperature model comparison with Yueh 2010 [18], for beam 1.

Figure 8 illustrate the modeled anisotropic effect of the relative wind direction at L-band for all beams and polarizations. For each incidence angle and polarization, this effect has more impact on the surface brightness temperature as wind speed increases. The figure also illustrates different response at different incidence angles and polarizations.

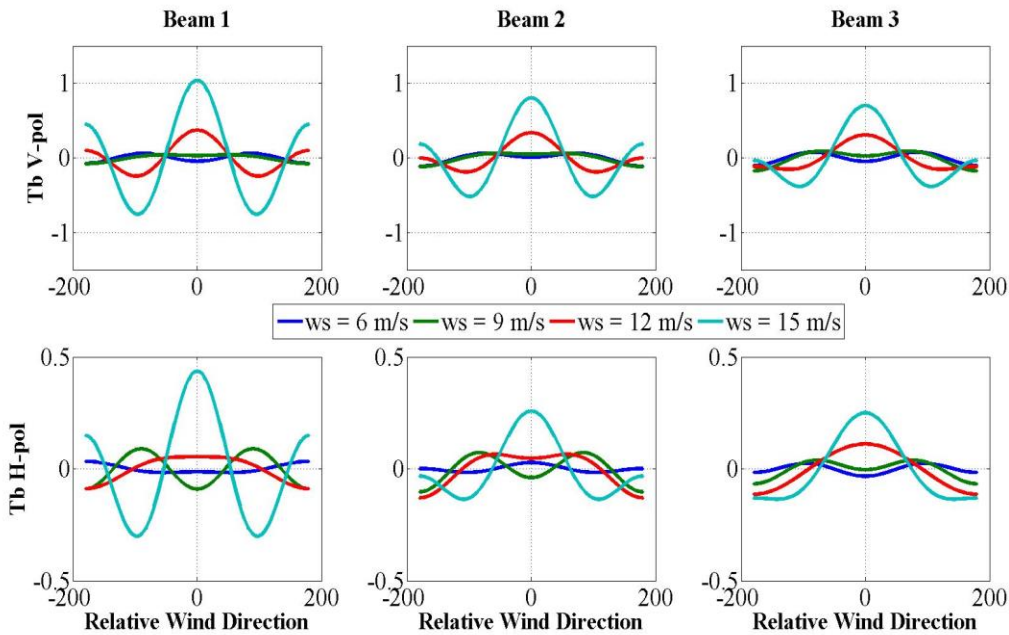


Figure 8 Modeling of the relative wind direction at L-band for four different wind speed values (6, 9, 12 and 15 m/s). The top three panels show results for beam 1 (left), beam 2 (middle) and beam 3 (right) for V-pol. The bottom three panels show results for beam 1 (left), beam 2 (middle) and beam 3 (right) for H-pol.

Figure 9 shows the comparison of the “goodness of fit” between the observed and the modeled surface Tb, for all values of sea surface temperature (273 – 305 K) and SSS (28 – 40 psu) as a function of relative wind direction for three different wind speed values (4, 8 and 15 m/s) for each beam and polarization. As discussed earlier, the mean value (DC-offset) of each curve is dependent on the wind speed value, and the dynamic range (standard deviation) is a function of relative wind direction at a constant wind speed. It is worth mentioning that the roughness effect is not a function of SST and SSS.

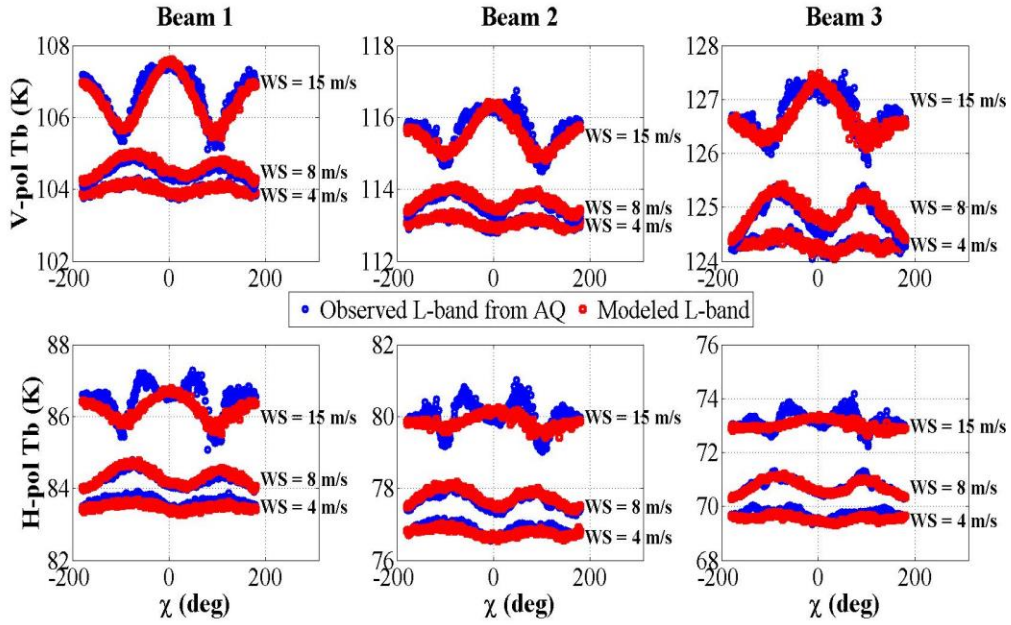


Figure 9 Correlation between L-band total observed (blue) and modeled (red) brightness temperature for each beam and polarization for the three incidence angles of Aquarius. Results are shown for three wind speed values namely; 4, 8 and 15 m/s.

As shown in Figure 5 and Figure 9, there is a high correlation between the modeled and the observed Tb, at different wind speed values and the full range of relative wind direction. The key indicator of the agreement between the two brightness temperatures is the RMS error. The total RMS errors, between the observations and the model, for all wind speed values between 0-20 m/s, are presented in Table 2.

3.2 Ka-Band Model Tuning

The first step in the tuning process is to build the match-up set. For this purpose, satellite radiometric data at Ka-Band for MWR, WindSat and SSMIS F17 (Special Sensor Microwave Imager/Sounder) are collocated at a spatial resolution of 0.25° to provide the model tuning match-up data set. For the radiometer data, the temporal match-up are $\leq \pm 1$ hour and the corresponding T_b 's are averaged in $0.25^\circ \times 0.25^\circ$ boxes. Data from either WindSat or SSMIS are collocated with MWR; whichever are closest in time are chosen for the final analysis. The advantage of using two different satellite data is to increase the number of collocated points as shown in Figure 10. The numerical weather model produced by the NOAA National Centers for Environmental Prediction (NCEP) is spatially interpolated and the temporal window is $\leq \pm 3$ hours. Match-up data from 2012 were used for tuning (~5,400,000 samples, from July 2012 – December 2012), and data from 2013 (9,500,000 samples from January 2013 – November 2013) were used for validation (see Chapter 6).

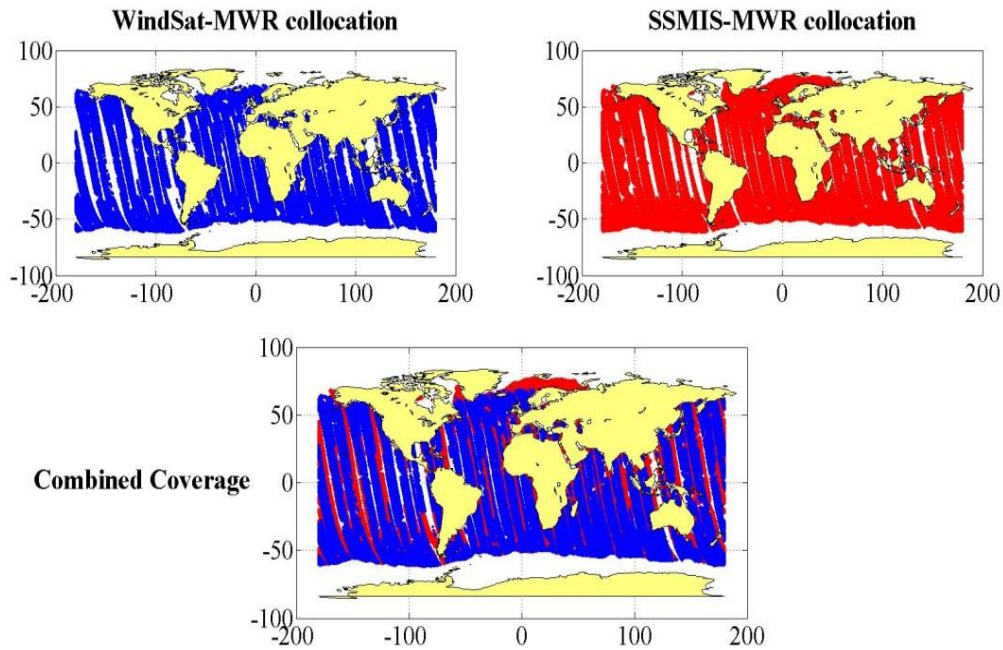


Figure 10 Ascending passes coverage of the collocations between MWR, SSMIS and WindSat data over one week period.

The CFRSL model tuning process at the Ka-band is performed using the above match-up data sources, namely; measured Ka-band brightness temperatures at the top of the atmosphere (TOA) MWR data product L-1B V7.0, environmental parameters from the National Centers for Environmental Prediction (NCEP), and WS, rain rate (RR) and cloud liquid water (CLW) retrievals from WindSat and SSMIS F17 provided by Remote Sensing Systems [19]. In a previous study [20], only brightness temperatures and NCEP environmental parameters were used to conduct this analysis, but the addition of simultaneous collocated ancillary data from WindSat and SSMIS improves the environmental parameter inputs for the theoretical radiative transfer model calculations.

Figure 11 shows the steps for tuning the Ka-band model.

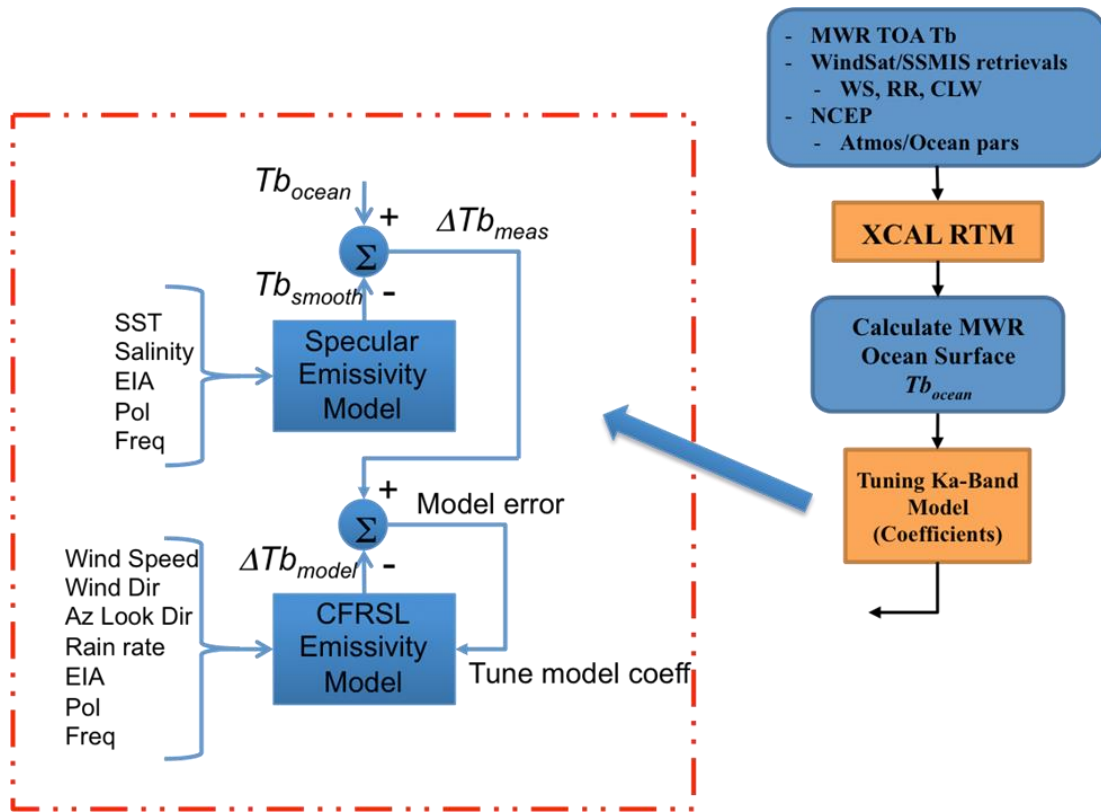


Figure 11 Tuning process for Ka-band model.

The next step in this process is to convert the MWR TOA Tb 's to the ocean surface brightness (Tb_{ocean}); and for this, an ocean microwave radiative transfer model (XCAL_RTМ) [21] is used. The inputs to this model are the following environmental parameters: NCEP atmospheric profiles of temperature, pressure and humidity, microwave radiometer retrievals of integrated CLW, WS and RR from the collocated WindSat and SSMIS, Reynolds SST and HYCOM SSS. The XCAL_RTМ is run for each collocation point, and the outputs are: the upwelling atmospheric brightness component (Tb_{up}), the downwelling atmospheric component (Tb_{dwn}), the ocean surface power reflection coefficient (r), and total atmospheric transmissivity (τ). Using these quantities

and reversing the radiative transfer model formula (*Appendix A*), the ocean surface Tb_{ocean} is found from,

$$Tb_{app} = Tb_{up} + \tau \times (Tb_{ocean} + \Gamma \times Tb_{down}) \quad (7)$$

For this analysis, only non-rainy scenes were used, and the near simultaneous rain rates provided by WindSat and SSMIS were used to filter (reject) these data.

3.2.1 Tuning Ka-Band Model For Wind Speed

After translating MWR TOA Tb 's to the surface, a non-linear fit was applied to estimate the coefficients of Equations (4) and (5) in the same manner that was used in the L-band modeling,

$$\varepsilon_{rough_{WS}}(EIA, WS, freq, SST) = (a_1 \times Z_{EIA} + a_2 \times Z_{WS} + a_3 \times Z_{EIA} \times Z_{WS}) \frac{\sqrt[4]{freq}}{SST}$$

$$\varepsilon_{rough_{WS}}(EIA, WS, freq, SST) = (a_0 + a_1 \times Z_{EIA} + a_2 \times Z_{WS} + a_3 \times Z_{EIA} \times Z_{WS}) \frac{\sqrt[4]{freq}}{SST}$$

that best reduces the RMS error, between the observed MWR ocean surface Tb and the estimated ocean surface brightness temperature (output of the CFRSL surface emissivity model). Coefficients were found iteratively for wind speeds between 0-20 m/s, which represent > 99% of all ocean wind speed values, as shown in the observed ocean wind speed histogram in Figure 12. The resulting coefficients are given in Table 3.

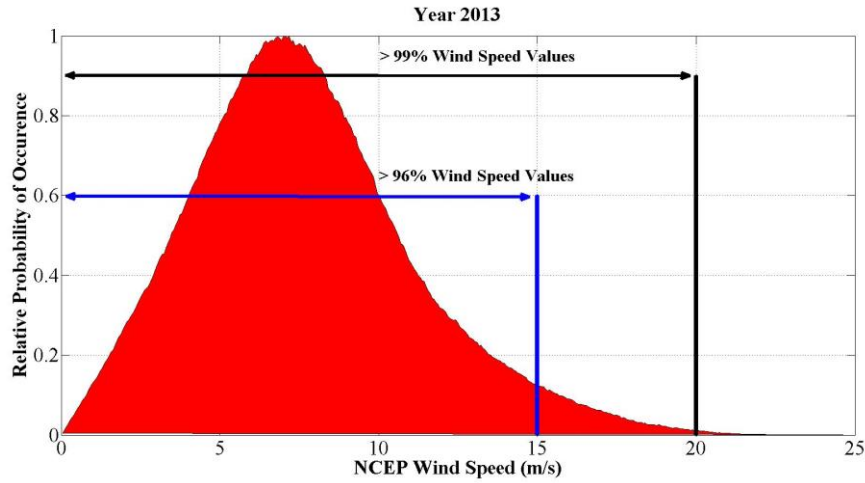


Figure 12 Relative probability of oceanic wind speed values for the year 2013 from AQ Level-2 data..

Table 3 Coefficients of wind speed effect model for Ka-band.

V-pol						H-pol					
Coef	Value	Coef	Value	Coef	Value	Coef	Value	Coef	Value	Coef	Value
a ₀	-0.186	b ₁	103.18	c ₁	3.617	--		b ₁	58.82	c ₁	11.39
a ₁	25.31	b ₂	33.99	c ₂	2.366	a ₁	1.138	b ₂	0.301	c ₂	5.554
a ₂	2.224	--	--	--	--	a ₂	12.18	--	--	--	--
a ₃	-154.42	--	--	--	--	a ₃	1.817	--	--	--	--

A comparison of the observed MWR surface Tb's with the tuned CFRSL model are shown in Figure 13, as a function of WindSat or SSMIS retrieved wind speed provided by RSS [19] and bin-averaged every 2 m/s. For the majority of the wind speeds ($WS \leq 20$ m/s), the modeled and the observed Tb's are highly correlated; but for wind speed values > 20 m/s, the number of samples is very low, which makes the fitting of the algorithm less certain. From this figure, it is observed that the CFRSL model fits H-pol better than V-pol. This is fortunate, because the greater dynamic range of the H-pol (~ 40 K) compared to the V-pol (~ 10 -15 K), results in the weighting of H-pol being higher in the estimate of the roughness correction.

Table 4 shows the RMS error between the modeled and measured Tb for each set of MWR beams, at different ranges of wind speeds. Note that the majority of the RMS error is associated with the wind direction anisotropy, which is corrected in the AQ excess roughness correction algorithm discussed in Section 4.1.

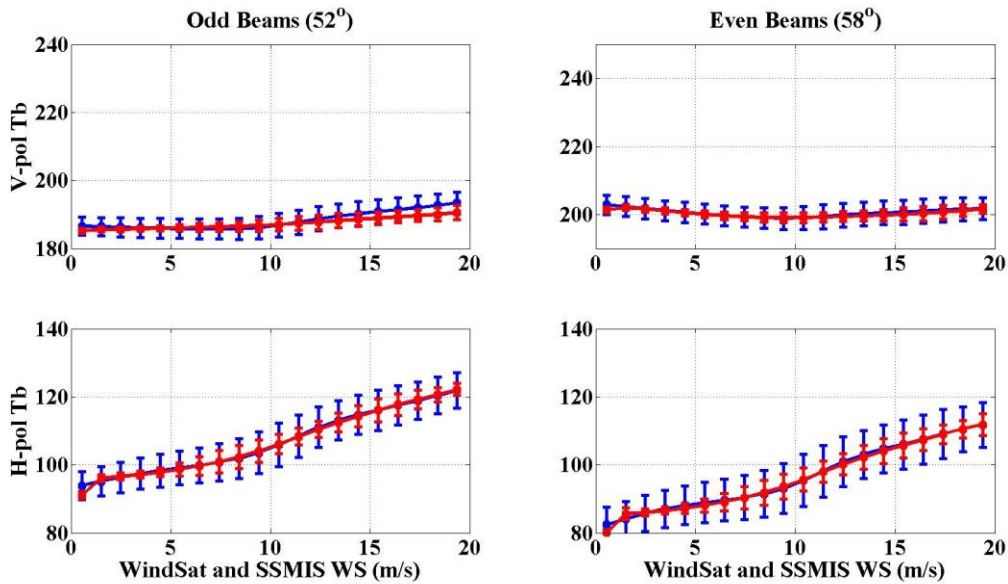


Figure 13 Bin average plots of modeled (red) 36.5 GHz and observed (blue) ocean surface brightness temperature at Ka-band. The top two panels show the results for the odd (left) and even (right) beams for V-pol. The bottom two panels show results for the odd (left) and the even (right) beams for H-pol.

Table 4 Root mean square error between measured and modeled brightness temperature at Ka-band for different ranges of wind speed.

Beams	RMS Error in Kelvin							
	0-5 m/s		5-10 m/s		10-15 m/s		15-20 m/s	
	V-pol	H-pol	V-pol	H-pol	V-pol	H-pol	V-pol	H-pol
Odd	1.51	2.45	2.67	4.72	1.91	3.29	0.79	1.26
Even	1.49	3.05	2.66	5.8	1.90	4.14	0.73	1.51

3.2.2 Tuning Ka-Band Model For Wind Direction

Using the same iterative technique, the β coefficients in Equation (3) were estimated, to model the zero-mean anisotropic relative wind direction effect, as a function of wind speed for both polarizations and MWR EIA's (odd and even beams). Figure 14 illustrates the wind speed dependence of the β coefficients for the MWR channels (V- and H-pol) and beams: even (EIA = 58°) and odd (EIA = 52°) and corresponding equations are presented in *Appendix E*.

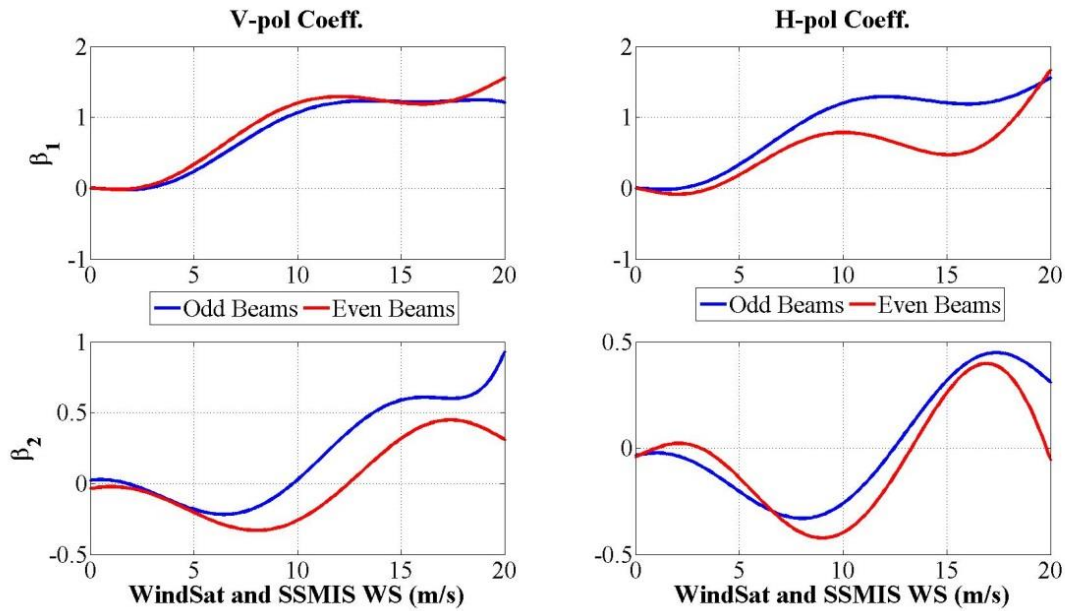


Figure 14 Ka-band β coefficients as function of wind speed for odd (blue) and even (red) beams. Top panel shows β_1 and bottom panel shows β_2 , and left panel shows the V- pol and right panel shows the H-pol.

Wentz [22] developed a model for the relative wind direction using data from the Special Microwave/Imager (SSM/I) collocated with buoy reports from the National Data Buoy Center (NDBC). The model showed results at a variety of frequencies and EIA; the closest had a frequency of 37 GHz and EIA of 53° . Comparisons with Wentz's model are shown in Figure 15

for wind speeds values of 6 and 10 m/s, which shows that there is a high level of similarity between both models for both polarizations. Also, as shown in the figure, the effect of relative wind direction will increase the standard deviation of the excess Tb (ΔT_b) by ~ 2 K at higher wind speeds.

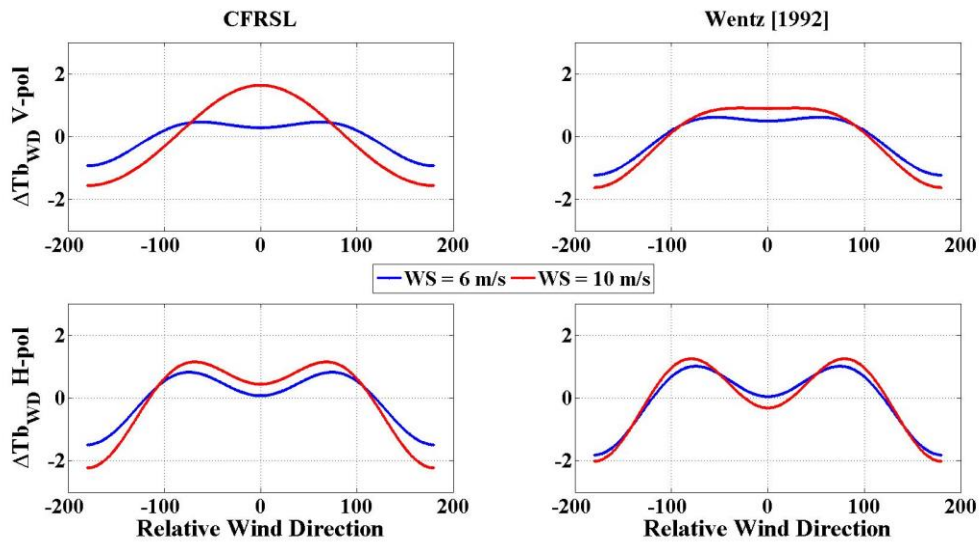


Figure 15 Ka-band wind direction model comparison for excess brightness temperature with Wentz 1992 [22], for odd beams.

Figure 16 illustrate the modeled anisotropic effect of the relative wind direction at Ka-band for all beams and polarizations. As the wind speed increase, this effect has more impact on the surface brightness temperatures at each incidence angle and polarization, and as illustrated in the figure, there is different response at different incidence angles and polarizations.

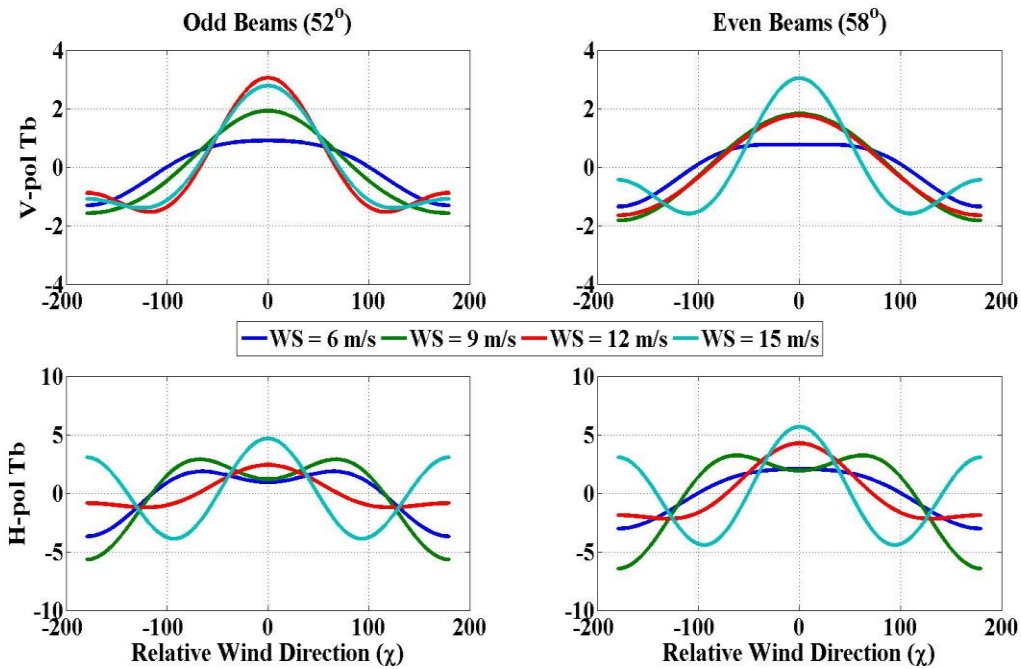


Figure 16 Modeling of the relative wind direction at Ka-band for four different wind speed values (6, 9, 12 and 15 m/s). The top two panels show results for odd beams (left) and even beams (right) for V-pol. The bottom two panels show corresponding results for odd beams (left) and even beams (right) for H-pol.

Figure 17 shows the “goodness of fit” between the observed and the modeled surface Tb, for all values of sea surface temperature (273 – 305 K) and SSS (28 – 40 psu) as a function of relative wind direction for wind speed values (6 and 10 m/s) for each beam group (EIA) and polarization. As shown in the figure, the mean value of each curve is dependent on the wind speed value, and the dynamic range is a function of relative wind direction. As in the L-band model, the roughness effect is not a function of SST and SSS.

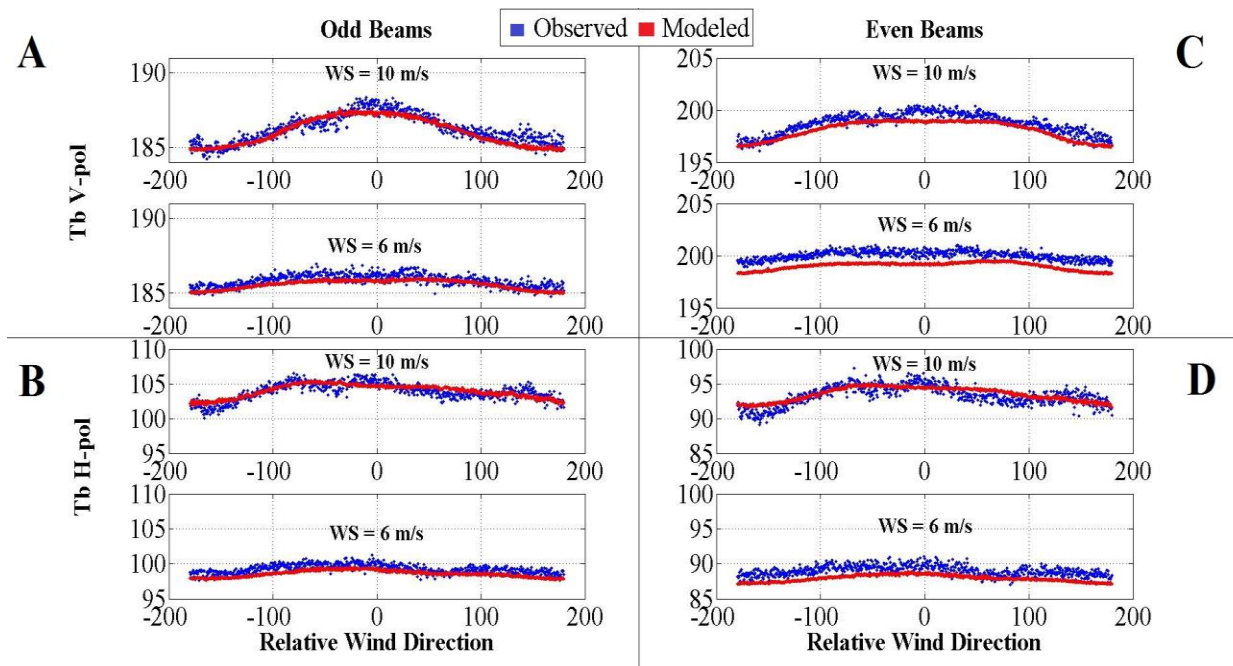


Figure 17 Correlation between the Ka-band total observed (blue) and modeled (red) ocean brightness temperature for each polarization and incidence angle of the MWR channels at two different wind speeds (6 and 10 m/s). Panel A: shows the V-pol for the odd beams; B: shows the H-pol for the odd beams; C: shows the corresponding V-pol for the even beams; and D: shows the H-pol for the even beams.

As illustrated in the figure, at each wind speed value, the mean value of the data points represents the off-set of the brightness temperature and changes with wind speed, while the dynamic range (standard deviation) changes with relative wind direction.

After modeling the isotropic roughness for both frequency band, a semi-empirical relationship between MWR Ka-band and AQ L-band excess Tb's using the MWR collocated data set (MWR, WindSat, SSMIS and GDAS), which is collocated in space and time with AQ data as shown in block diagram in Figure 18. This empirical relationship will be discussed in depth in Chapter 4.

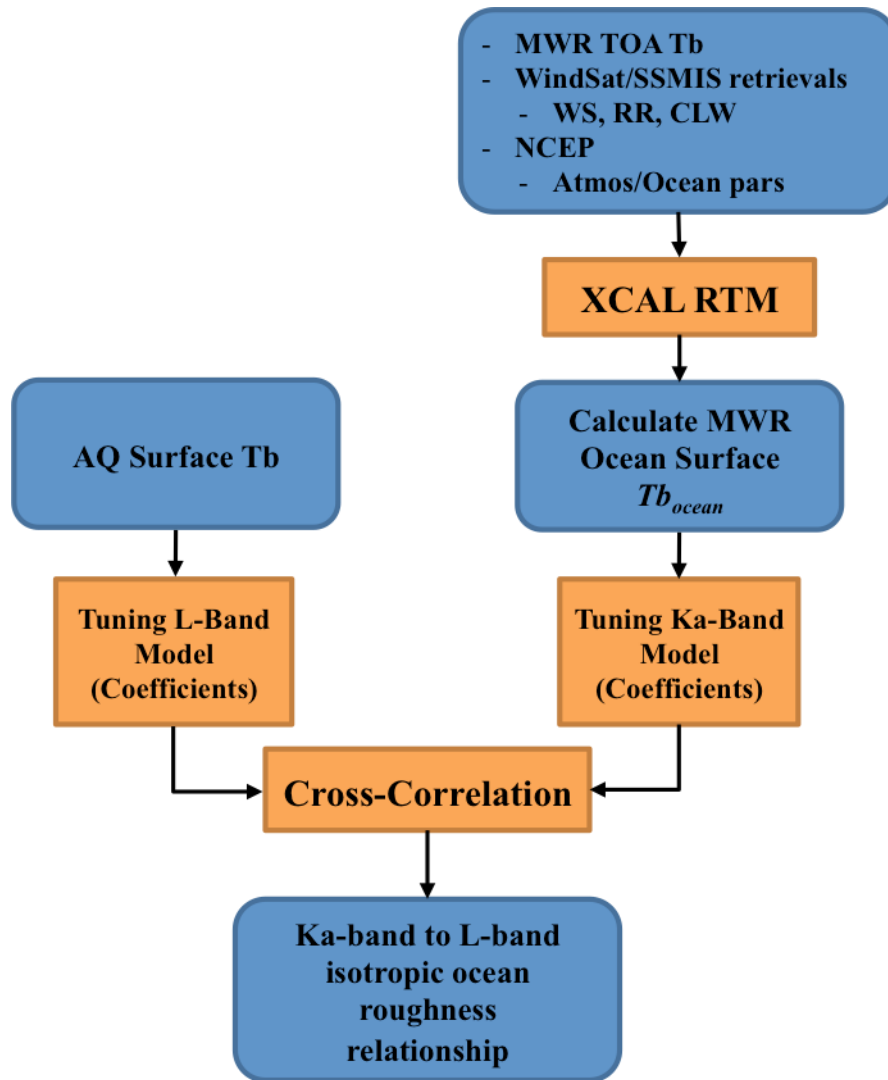


Figure 18 Block diagram of the process of generating a cross-correlation between isotropic roughness at Ka-band and at L-band.

CHAPTER 4: AQUARIUS OCEAN ROUGHNESS CORRECTION

Aquarius sea surface salinity retrieval requires knowledge of the specular (smooth surface) ocean emissivity (ϵ_{smooth}) at L-band (1.413 GHz) for V- and H-pol. Conceptually, this is achieved by subtracting the ocean roughness correction (excess Tb) from the total measured ocean surface Tb (provided in the AQ L-2 V3.0 science data product) to yield the specular (smooth ocean) Tb. This process, called *Ocean Roughness Correction*, will be described in depth in the following Chapter. The final step in calculating specular ocean emissivity is to divide the specular ocean Tb by the SST.

The baseline roughness correction for AQ is derived from the onboard scatterometer polarized ocean backscatter measurement cross-correlation with the L-Band excess Tb (*Appendix F*). This dissertation produces an alternative roughness correction approach using MWR Tb measurements at Ka-band with the tuned CFRSL model and with NCEP surface wind directions.

4.1 MWR Roughness Correction

The MWR roughness correction algorithm is based upon the cross-correlation between MWR Ka-band and AQ L-band excess Tb's. This semi-empirical relationship is developed using the MWR collocated match-up data set (MWR, WindSat, SSMIS and GDAS), which is collocated in space and time with AQ data. Due to the difference in geometry between each AQ beam and each set of MWR beams (odd and even beams), the collocation is done by separating the MWR beams that fall inside the AQ IFOV's by incidence angle (beam #'s).

Weighted averaging was applied to MWR observations that fall inside each AQ IFOV separately based on the incidence angle and the polarization. Figure 19 illustrates the geometry of the AQ and MWR beams. As shown in the figure, each AQ IFOV encircles two or three MWR beams from different incidence angles and azimuth angles, and therefore the weighted averaging has been done for each group of the MWR beams separately.

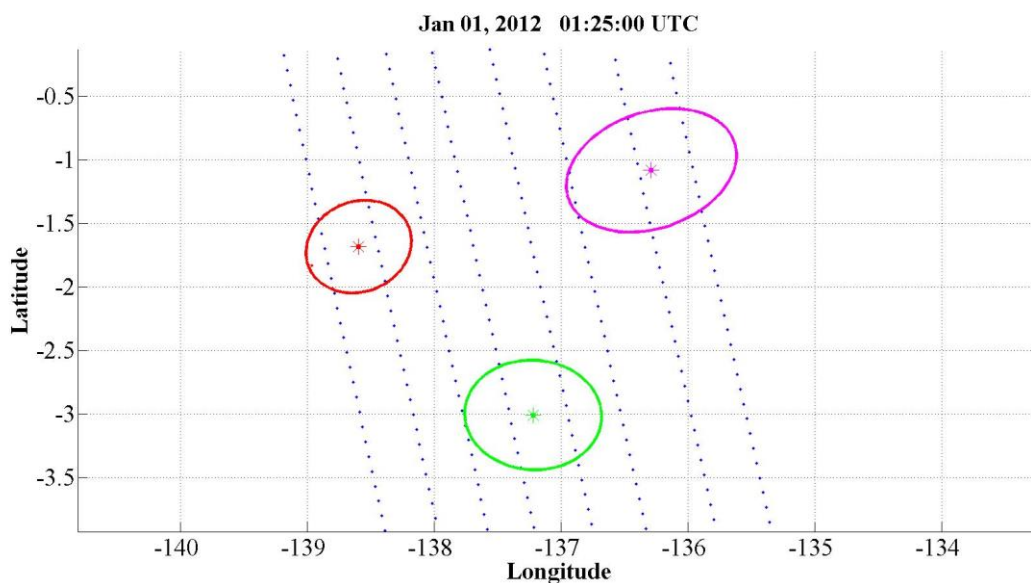


Figure 19 MicroWave Radiometer and Aquarius swath collocation. MWR 8 beams (blue dots) share the same swath with the three Aquarius beams; inner (red), middle (green) and outer (magenta).

Figure 20 represents a Google Earth image of the modeled IFOV of AQ and MWR provided by CONAE. The green arrows are the line of sight directions respectively for the AQ beam-1 and for the MWR beam-1. This illustrates the difference in the azimuth angles (relative to the sub-satellite point when measured CW from the North); and these azimuth differences translate to different relative wind directions (*Appendix E*) at each AQ and each MWR IFOV's. Since there are different MWR beams that are used to make a wind direction adjustment in the AQ excess

roughness correction for a given AQ beam, these different relative wind directions must be carefully taken into account.

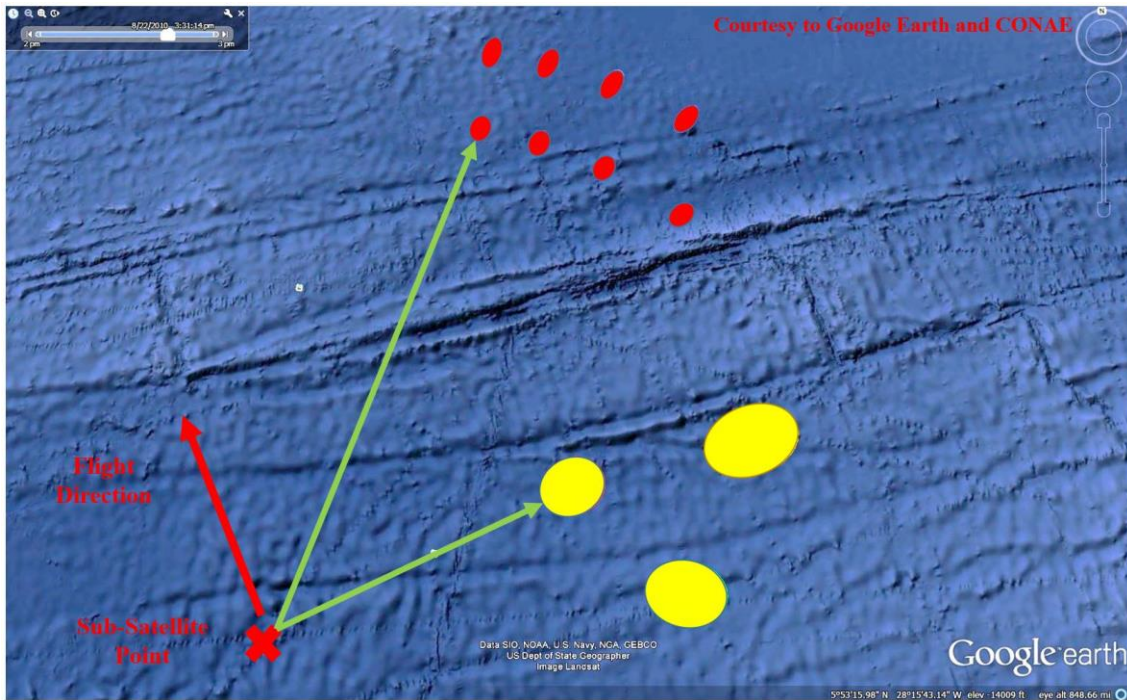


Figure 20 Google Earth image of Aquarius and MicroWave Radiometer beams, showing the difference in azimuth angle, which corresponds to difference in the relative wind direction angle.

4.1.1 AQ/MWR Forward Isotropic RTM

To convert the Ka-band roughness to L-band, an empirical relationship (forward RTM) was found for every AQ polarization and EIA (beam #). Further, since the geometry (azimuth viewing direction) of the beams is different between the various AQ and MWR IFOV's, the anisotropic wind direction compensation of the CFRSL model (ΔTb_{WD}) will be different on each of the measured Tb 's (because of the difference in relative wind directions, EIA, frequency and

polarization). This wind direction effect was subtracted leaving only the isotropic wind speed effect (isotropic roughness, ΔTb_{WS}) as follows,

$$\Delta Tb_{WS} = \Delta Tb_{total} - \Delta Tb_{WD} \quad (8)$$

So to develop the forward model, the isotropic excess Tb is found for each AQ beam collocation. Here collocated L-band and Ka-band beams were wind direction corrected by applying Equation (8) and then averaged over the AQ footprints to produce one isotropic excess Tb sample for an associated scatterometer surface wind speed (from AQ L-2). This resulted in > 1M observations over wind speeds that were combined in a statistical regression model for six AQ beams and pol. This resulting empirical forward model relationship was established to convert the isotropic Ka-band excess Tb to the corresponding isotropic L-band excess Tb. For each AQ beam there is a different combination of MWR (odd and even) beams that are averaged to form this relationship. Figure 21 shows a binned-average (mean and standard deviation) scatter plot that represents these 6 forward models.

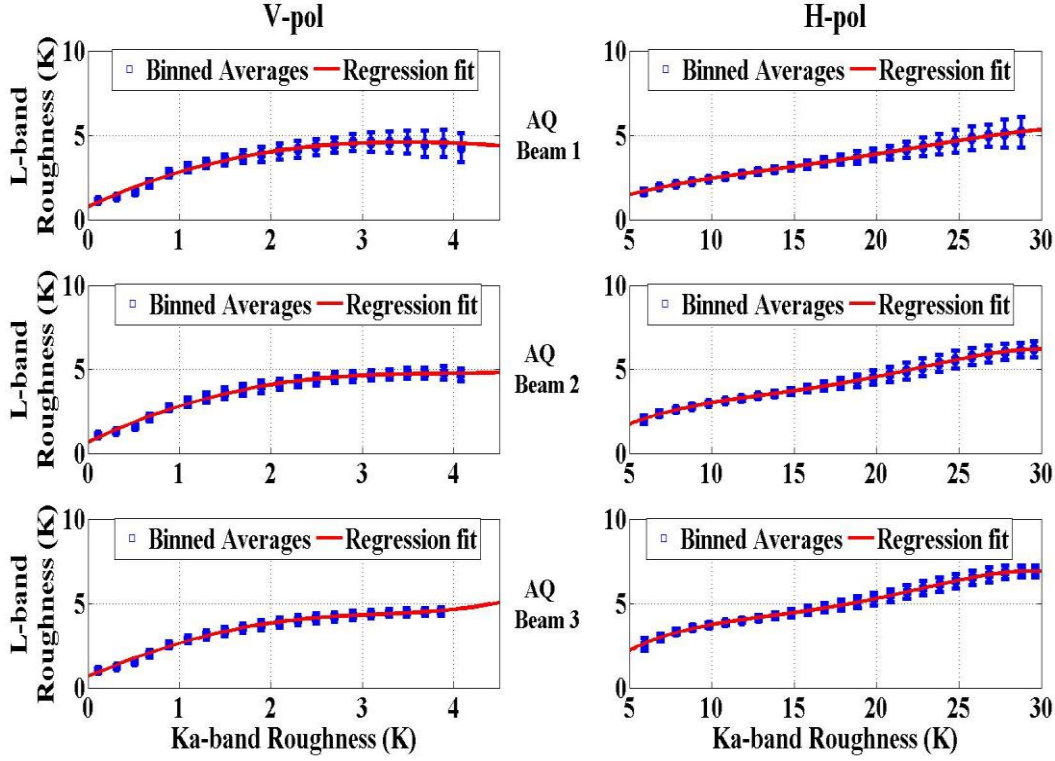


Figure 21 Forward models between the roughness correction at Ka-band and L-band by AQ beam#. Left panels represent the vertical polarization and right panels represent the horizontal polarization.

As the figure illustrates, the V-pol L-band measured roughness saturates at higher values of wind speeds, while the H-pol L-band roughness increases monotonically with wind speed. A fourth-order polynomial regression fit was applied to generate an empirical relationship that translate the isotropic Ka-band roughness to isotropic L-band roughness, and can be expressed as follows,

$$\Delta T b_{L,p,B} = a_4 \Delta T b_{Ka,p}^4 + a_3 \Delta T b_{Ka,p}^3 + a_2 \Delta T b_{Ka,p}^2 + a_1 \Delta T b_{Ka,p} + a_0 \quad (9)$$

where $\Delta Tb_{L,p,B}$ is the isotropic roughness at L-band frequency (L), $\Delta Tb_{Ka,p}$ is the isotropic roughness at Ka-band frequency (Ka), p indicates the polarization and B is AQ beam number ($B = 1:3$). The coefficients a are presented in Table 5.

Table 5 Coefficients of the conversion formula from Ka-band roughness to L-band roughness.

Pol/Beam number	a4	a3	a2	a1	a0
V-1	-5×10^{-16}	0.02	-0.50	2.53	0.74
V-2	0.008	-0.03	-0.39	2.54	0.65
V-3	0.02	-0.12	-0.15	2.22	0.66
H-1	-1.6×10^{-5}	0.001	-0.03	0.47	-0.25
H-2	-4.4×10^{-5}	0.003	-0.08	0.98	-1.56
H-3	-5.8×10^{-5}	0.004	-0.10	1.28	-2.03

4.2 AQ Roughness Correction Algorithm

The AQ excess roughness retrieval algorithm uses measured NCEP wind directions with MWR TOA Tb's to calculate corresponding L-band excess roughness correction. The algorithm conceptual block diagram is shown in Figure 22.

First the MWR TOA Tb's are converted to the surface using collocated NCEP and WindSat/SSMIS environmental parameters and running the XCAL RTM. Then, the observed MWR excess Tb is calculated by removing the smooth water emissivity using ancillary SST and HYCOM SSS data from the AQ L-2 data. Next the relative wind directions are calculated for the AQ and MWR IFOV's using NCEP wind directions and the AQ/MWR azimuth measurement geometry (see *Appendix E*). Then, a Ka-band wind direction correction is made (Equation (8)) to produce the MWR observed isotropic excess Tb, which is input into the forward model to produce the equivalent L-band isotropic excess Tb. Finally, the relative wind direction at the AQ IFOV is

used to calculate the corresponding L-band wind direction effect, which is added to the isotropic excess Tb. This summation results in the AQ excess roughness correction ($\Delta T_{b_{WS,WD}}$) that accounts for both wind speed and wind direction effects.

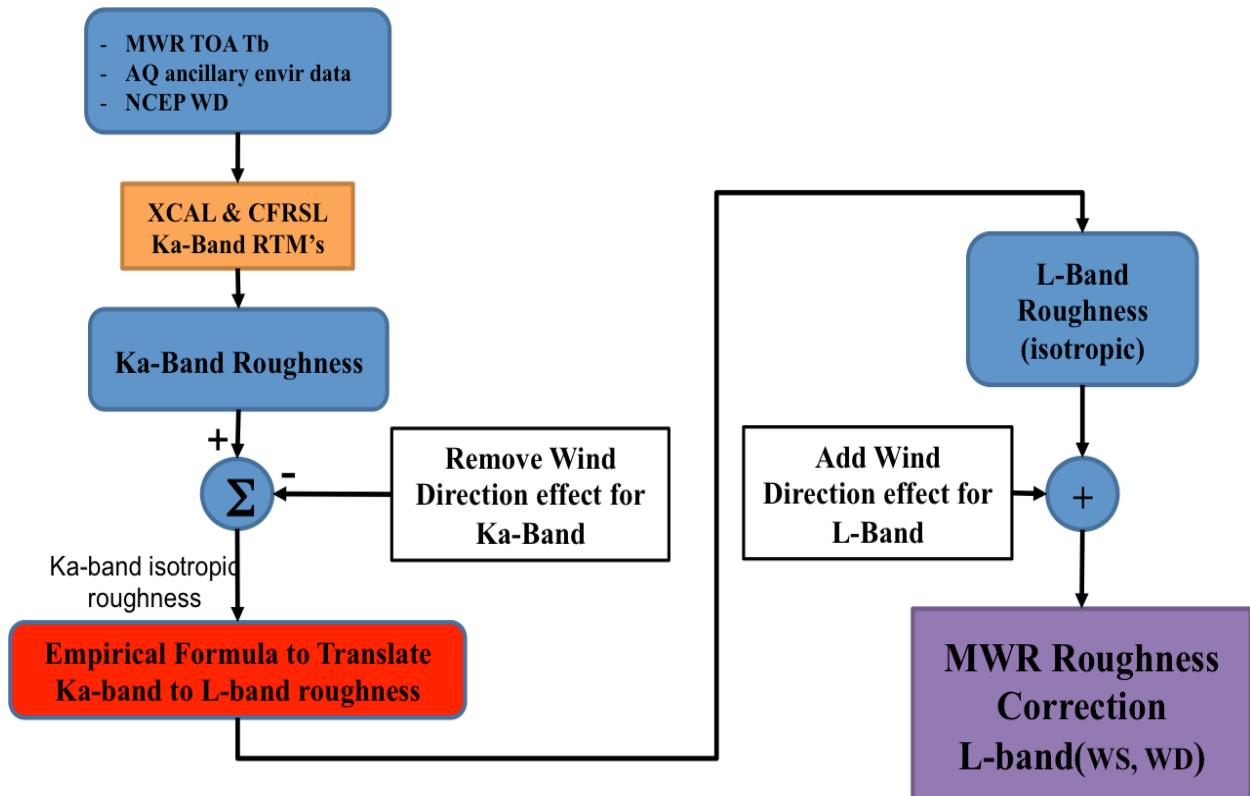


Figure 22 The process of calculating the MWR roughness correction.

4.3 MWR-Derived Roughness Correction Comparison

Comparisons (mean and standard deviation) between the scatterometer-derived roughness (binned-averages in blue) and MWR-derived roughness (binned-averages in red), for both polarizations for the three AQ beams, are presented in Figure 23. As shown in the figure, there is high correspondence between both excess Tb's. Note the high STD at high wind speeds is probably

related to the stronger wind direction effects. Since the scatterometer roughness correction is independently derived, it is difficult to draw many conclusions as to which is better.

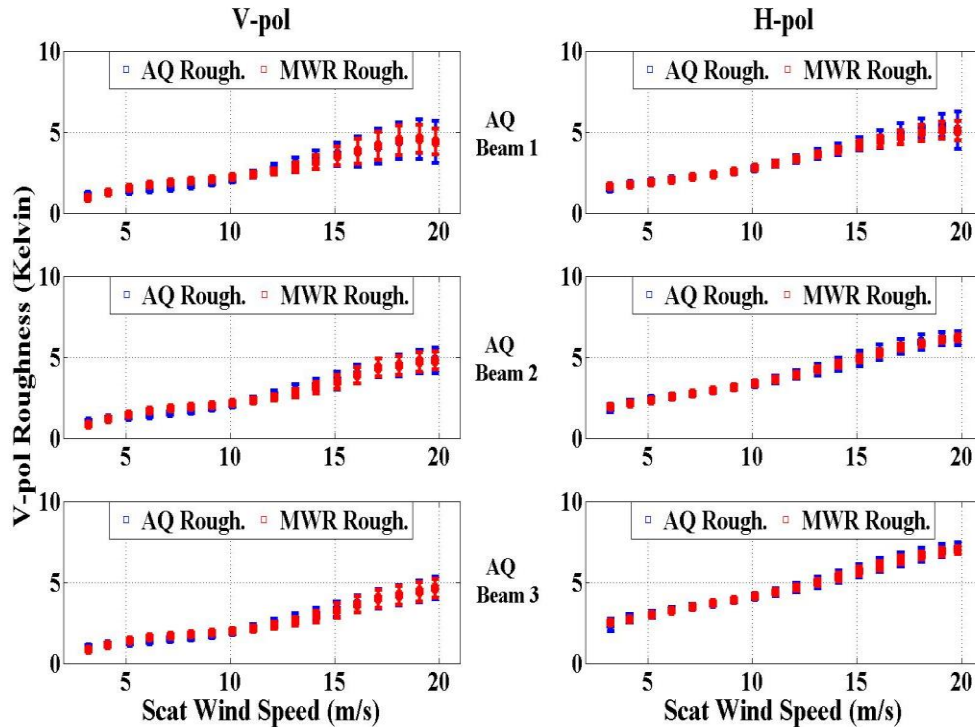


Figure 23 Aquarius scatterometer derived roughness (blue) and MWR derived roughness (red). Left panels represent the vertical polarization and right panels represent the horizontal polarization. First row represents Aquarius beam 1, second row represents Aquarius beam 2 and the third row represents Aquarius beam 3.

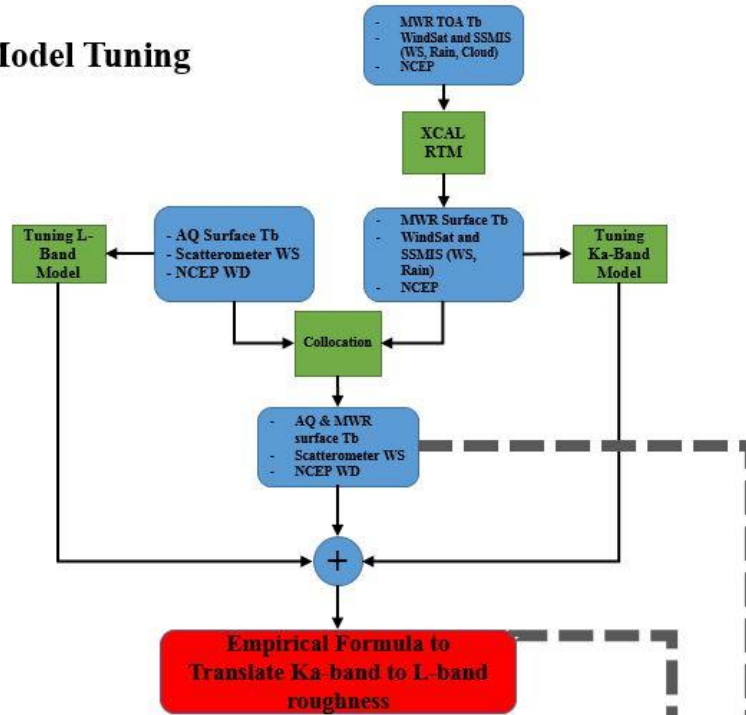
However, in Chapter 6, each of the two roughness corrections (scatterometer roughness correction and MWR roughness correction), are implemented, and used to retrieve SSS, and there results are compared and evaluated. Then, the AQ roughness correction is implemented by simply subtracting the calculated excess T_b from the measured brightness temperature to obtain the smooth surface T_b ,

$$Tb_{smooth} = Tb_{measured} - \Delta Tb_{WS,WD} \quad (10)$$

The resulting smooth Tb does not have any dependence on wind speed or relative wind direction and is entirely a function of frequency, EIA, SST and SSS. The only unknown now is the SSS, and to solve for it, the salinity retrieval algorithm discussed in Chapter 5 was applied.

Figure 24 shows a flow chart of the tuning and the roughness correction process.

CFRSL Model Tuning



CFRSL Roughness

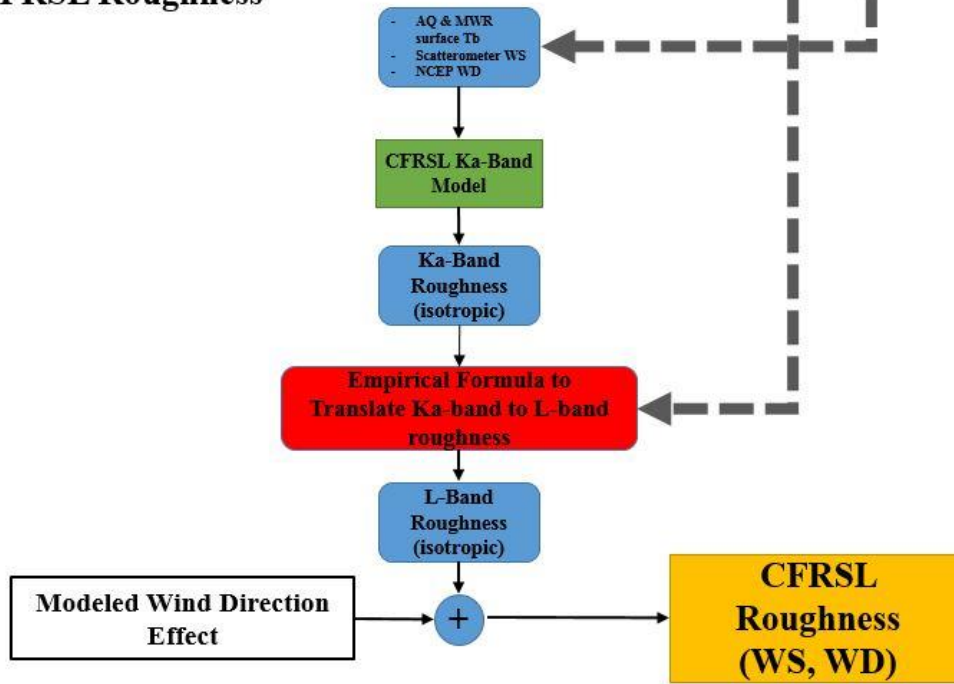


Figure 24 Flow chart of the roughness correction process

CHAPTER 5: SEA SURFACE SALINITY

Oceans cover over 70% of the earth's surface and that is where 87% of the global evaporation and 78% of the global precipitation occur [23], and these changes in the freshwater content reflect on the salt content of the body of water causing changes in SSS. Therefore, AQ objective is to generate global weekly maps of SSS to monitor the seasonal and annual variation, with an accuracy of 0.2 psu (practical salinity unit [24]). To achieve this accuracy in SSS measurement, AQ needs to accurately measure the surface Tb by correcting for other sources of error (unwanted signals), yielding Tb measurement that is only a function of SSS and SST (*Appendix A*). And while the SST is well monitored, the only unknown in the measured surface Tb is SSS which can be easily retrieved at this point.

Figure 25 shows the change of surface Tb with SST, at constant values of SSS using the dielectric model [13]. The majority of open ocean sea surface salinity values fall between ~32 – 37 psu [4].

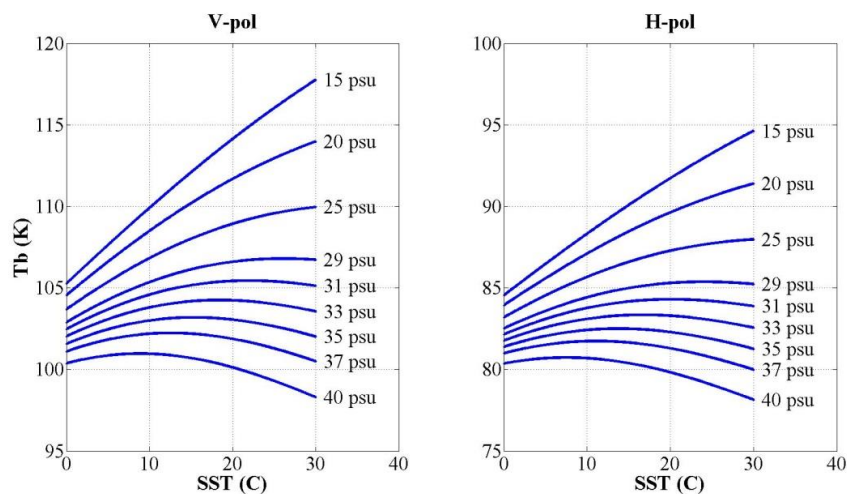


Figure 25 Brightness temperature as a function of sea surface temperature at different constant salinity.

5.1 Salinity Retrieval Algorithm

As mentioned previously, changes in SSS can be reflected on the sea surface emissivity, when measured at L-band frequency. The major difficulty is that the salinity signal is extremely weak and is prone to various error sources when measured from space; mainly, instrumental and geophysical radiometric errors that can affect the measured T_b . The monthly accuracy of AQ retrieved SSS is required to be 0.2 psu and that can only be achieved if the total root sum square (RSS) of all T_b measurement errors, at each observation, is less or equal to 0.38 K. The allocation of every error source and the pre-launch current best estimate (CBE) are shown in Table 6 [2]. By removing all sources of error, the remainder signal is the surface smooth T_b , which is solely a function of SST and SSS at a specific EIA, and polarization.

For a known SST, the process of retrieving SSS is a direct approach that uses experimental understanding of the behavior of the seawater complex dielectric constant to changes in SSS at 1.4 GHz and theoretical understanding of Fresnel reflection coefficient at different frequencies and EIA's.

Table 6 Aquarius salinity retrieval error table [2].

Error Sources	3 Beam RMS	
	Allocation	CBE
Radiometer	0.15	0.09
Antenna	0.08	0.01
System Pointing	0.05	0.02
Roughness	0.28	0.20
Solar	0.05	0.02
Galactic	0.05	0.004
Rain (Total Liquid Water)	0.02	0.01
Ionosphere	0.06	0.043
Atmosphere (Other)	0.05	0.02
SST	0.10	0.07
Antenna Gain Near Land & Ice	0.10	0.10
Model Function	0.08	0.07
Brightness Temperature Error Per Observation	Baseline Mission	
	Allocation	CBE
Total RSS (K)	0.38	0.27

The correction of unwanted Tb contributions is a tedious subtractive process in which the signal from unwanted sources of radiation (galaxy, sun moon, atmosphere and ionosphere) is removed from the measured apparent brightness temperature (T_{app}), which is the brightness temperature at the input of the feed horns (top of atmosphere) [25]. Figure 26 shows the sources of brightness temperatures in the received signal by AQ. After removing the effects of the ionosphere (which causes polar mixing), there are a series of corrections that follow, namely: galaxy (direct radiation and reflected radiation of the surface of earth), solar radiation (direct and reflected), and lunar reflected radiation. The remaining signal is the apparent Tb of earth ($T_{app,earth}$) that can be expressed as,

$$T_{app,earth} = T_{app} - T_{gal_{dir}} - T_{gal_{ref}} - T_{sun_{dir}} - T_{sun_{ref}} - T_{sun_{bak}} - T_{mon_{ref}} \quad (11)$$

where $T_{app,earth}$ is the temperature of earth at the top of the atmosphere, $T_{gal_{dir}}$ is the direct galactic signal, $T_{gal_{ref}}$ is the reflected galactic signal, $T_{sun_{dir}}$ is the direct solar signal, $T_{sun_{ref}}$ is the reflected solar signal, $T_{sun_{bak}}$ is the solar backscattered signal and $T_{mon_{ref}}$ is the reflected lunar signal. The result of Equation (11) represents the brightness temperature at the top of the atmosphere emitted by earth, and this includes Tb_{ocean} , Tb_{up} and reflected Tb_{dwn} . The surface brightness temperature is finally calculated using the Radiative Transfer Theory [26] by reversing Equation (7) as,

$$Tb_{ocean} = \frac{Tb_{app} - Tb_{up}}{\tau} - \Gamma \times Tb_{dwn} \quad (12)$$

The data processing algorithms to provide this Tb_{ocean} is the responsibility of the AQ project and is performed by Remote Sensing Systems [25, 27]. The the time series of Tb_{ocean} and other ancillary data (e.g. AQ measurement latitude/longitude, beam number, sea surface temperature, surface wind speed, etc) is provided by NASA JPL PODAAC [28] on an orbital basis, as the AQ science data product L-2 V3.0, which is the starting point for this dissertation.

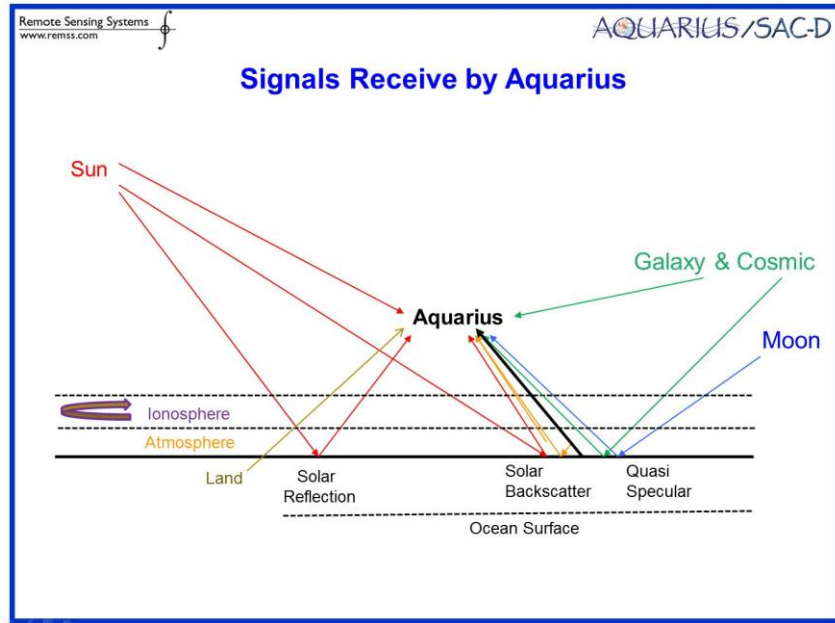


Figure 26 Signal received by Aquarius [19].

Before the AQ SSS retrieval, the “smooth” ocean surface T_b must be determined. This involves the removal of the rough ocean “excess T_b ” that corrects the effect of wind speed and wind direction, and for that, the baseline approach for AQ is to use excess T_b derived from the Aquarius scatterometer. For this correction, the scatterometer VV-pol backscatter and the ancillary significant wave height (SWH) are used to calculate the effect of wind speeds and wind direction ($\Delta\epsilon_{rough}$) [27].

The specular emissivity is calculated by subtracting the rough emissivity,

$$\epsilon_{smooth} = \epsilon_{ocean} - \Delta\epsilon_{rough} \quad (13)$$

And by simply multiplying the output of Equation (13) by SST, the specular brightness temperature that is used to retrieve SSS can be obtained as,

$$Tb_{smooth} = \epsilon_{smooth} \times SST \quad (14)$$

After obtaining the surface Tb, the salinity is found in an iterative manner using a maximum likelihood estimate (MLE) that reduces the difference between the measured brightness temperature (Tb^{mea}) and the modeled brightness temperature (Tb^{RTM}) [27]. The Tb^{RTM} is found by calculating the complex sea water dielectric constant using the *Meissner and Wentz dielectric model* [13], and measuring the Fresnel reflection coefficients using Equations (21) and (22) (refer to *Appendix A*). The MLE is expressed as follows,

$$MLE^2 = \frac{[Tb_V^{mea} - Tb_V^{RTM}]^2}{var(Tb_V)} + \frac{[Tb_H^{mea} - Tb_H^{RTM}]^2}{var(Tb_H)} \quad (15)$$

where $var(Tb_V)$ and $var(Tb_H)$ are the expected variance (standard deviation) between the measured polarized Tbs and the expected surface Tb.

5.2 Hybrid Coordinate Ocean Model (HYCOM) Salinity

HYCOM is a collaborative program by the U.S. Navy at Naval Oceanographic Office (NAVOCEANO), the Fleet Numerical Meteorology and Oceanography Center (FNMOC) and NOAA at the National Centers for Environmental Predictions (NCEP), to develop an oceanographic model to provide real-time global and basin-scale environmental salinity and other geophysical parameters [29].

HYCOM salinity is a product of this model that is produced daily on a global scale, by collecting in-situ surface temperature as well as in-situ vertical temperatures and salinity profiles from ARGO floats and mooring buoys.

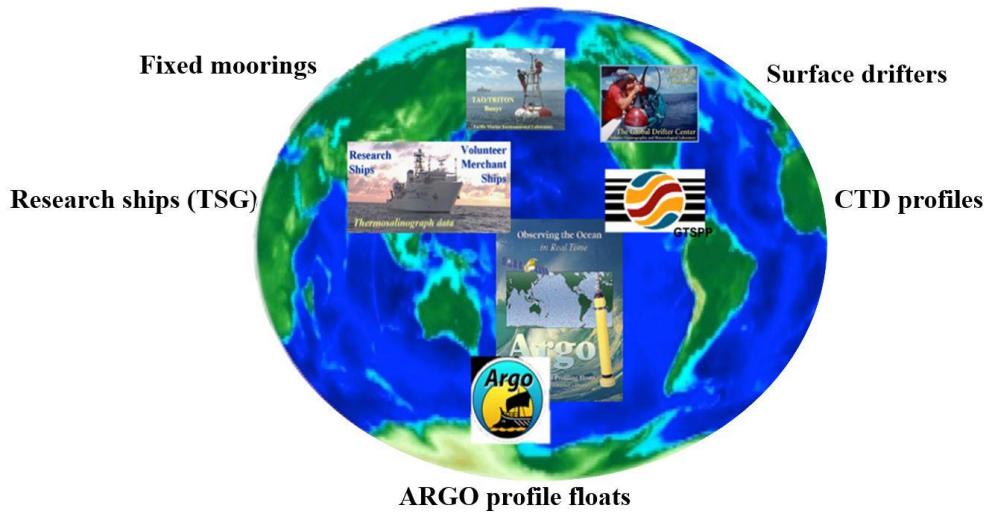


Figure 27 HYCOM In-Situ data sources.

The model interpolates the data points zonally and vertically and takes into account the mixing of layers over time to generate a salinity product that covers the globe every twenty four hours, with a spatial resolution of $1/12^\circ$ (at ~ 10 m depth). The advantage of this model over the physical readings, is the availability every twenty four hours and a 100% global coverage, which cannot be provided by physical measurements. This makes HYCOM a reliable source of bulk ocean salinity estimates (at ~ 10 m depth) that are representative of the SSS values for rain free scenes [30]. Figure 28 shows a global 24-hours average of HYCOM salinity [31]

SSS Jan 02, 2014 00Z 91.1

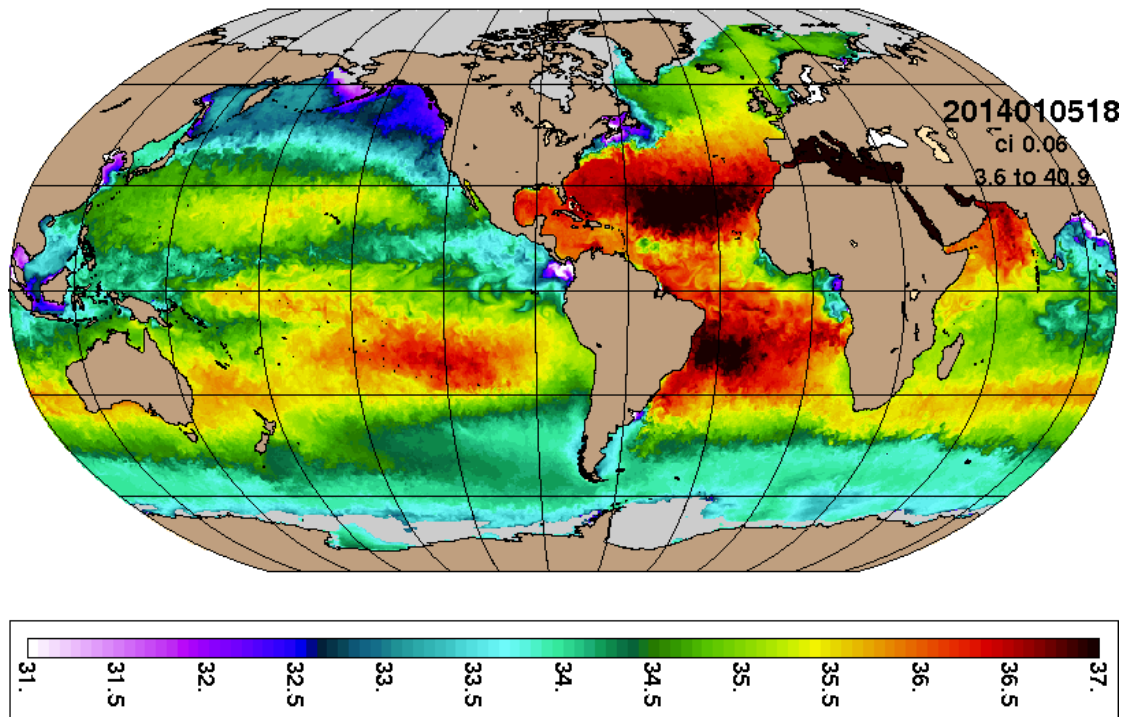


Figure 28 Six hours average of HYCOM salinity on January 2nd, 2014 [31].

The AQ data processing system collocates the HYCOM salinity in space and time with each AQ footprint measurement every 1.44 second, to be used as a reference for the salinity retrievals. In Chapter 6, comparisons between the AQ salinity (using both scatterometer and MWR derived roughness corrections) and HYCOM salinity are presented for rain free scenes, where the effects of surface salinity gradients (stratification) do not exist.

CHAPTER 6: RESULTS AND VALIDATION

6.1 CFRSL Retrieved Salinity

This dissertation addresses the improvement of the AQ salinity retrievals by comparing retrieval SSS using baseline (SCAT) and MWR roughness corrections. Both sets of SSS are compared to HYCOM and cross-correlated against oceanic winds (speed & direction). For these cases, the same salinity retrieval algorithm used by the AQ data processing system was adopted, and therefore differences in results can be attributed to the two roughness corrections used.

The SSS retrievals for the two techniques; scatterometer-derived roughness and MWR roughness corrections, are compared to HYCOM SSS by calculating the difference salinity (ΔSSS) as follows,

$$\Delta SSS = \mathit{Retrieved}_{SSS} - \mathit{HYCOM}_{SSS} \quad (16)$$

where HYCOM_{SSS} is HYCOM salinity and $\mathit{Retrieved}_{SSS}$ is the SSS derived using the MWR roughness correction for the first case and the SSS derived from the scatterometer roughness correction for the second case. The mean and standard deviation of ΔSSS for the two cases of are shown in Figure 29.

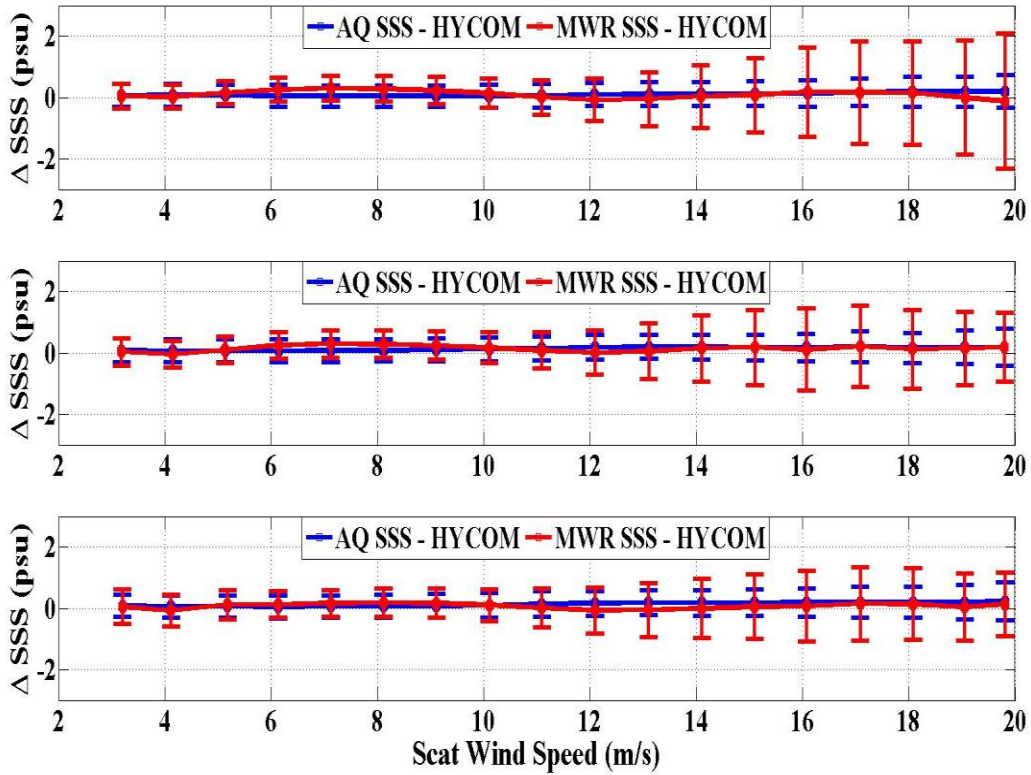


Figure 29 Difference between AQ salinity and HYCOM (blue) and MWR salinity and HYCOM (red). First row represents Aquarius beam 1, second row represents Aquarius beam 2 and the third row represents Aquarius beam 3.

Over the full range of wind speeds, Δ SSS does not have any significant dependence on the scatterometer wind speed. Table 7 shows the mean and the standard deviation values of the difference between MWR-derived SSS and $\text{HYCOM}_{\text{SSS}}$, at different ranges of wind speed for the entire year of 2013 for each AQ beam. The global mean value for each of the three beams for wind speeds less than 15 m/s is less than 0.2 psu (meets the requirement). Standard deviation of the differences is caused by wind direction. It is worth mentioning that HYCOM provides SSS at ~ 10 m depth, while microwave radiometry provides measurements at few centimeters depth, and they can have effects on the differences.

The relatively higher global mean and standard deviation is caused during events with wind speed values higher than 15 m/s, as shown in table for each beam; and the reason for that is that there is a significant reduction in the number of observations that are used for the tuning process.

Table 7 Mean and standard deviation of the difference between MWR derived salinity and HYCOM salinity at different ranges of wind speed.

Beam Number	Mean Value (psu)				Standard Deviation Value (psu)			
	0 – 5 m/s	5 – 10 m/s	10 – 15 m/s	15 – 20 m/s	0 – 5 m/s	5 – 10 m/s	10 – 15 m/s	15 – 20 m/s
Beam 1	0.09	0.09	-0.01	-0.06	0.50	0.47	0.67	0.94
Beam 2	0.10	0.13	0.04	-0.15	0.53	0.50	0.68	0.92
Beam 3	0.10	0.07	-0.03	-0.27	0.56	0.51	0.68	0.87

On a global scale, there is no systematic difference in behavior between the two salinity retrievals as shown in Figure 30 and Figure 31 that show global maps of ΔSSS_{AQ} and ΔSSS_{MWR} , respectively.

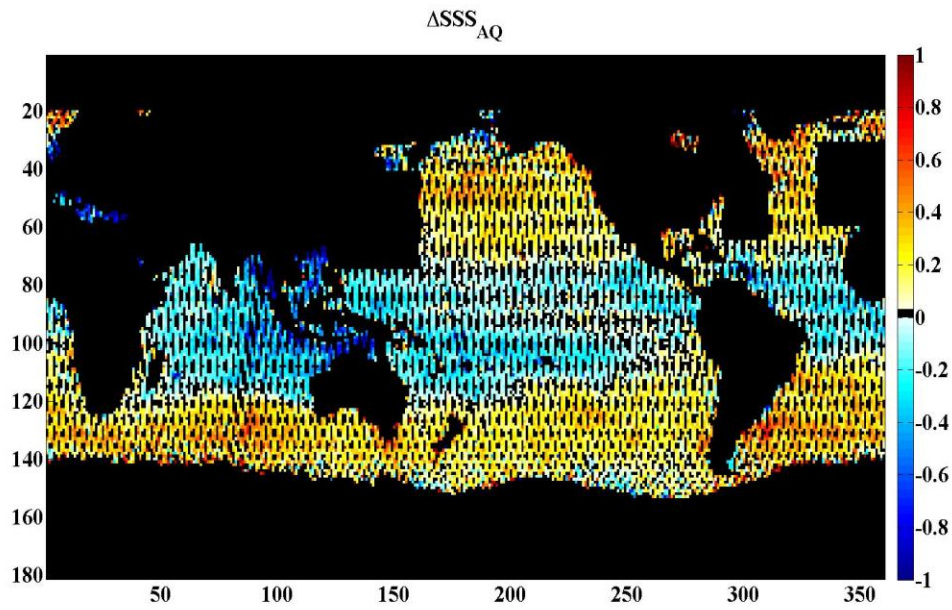


Figure 30 Global delta sea surface salinity derived using scatterometer roughness correction.

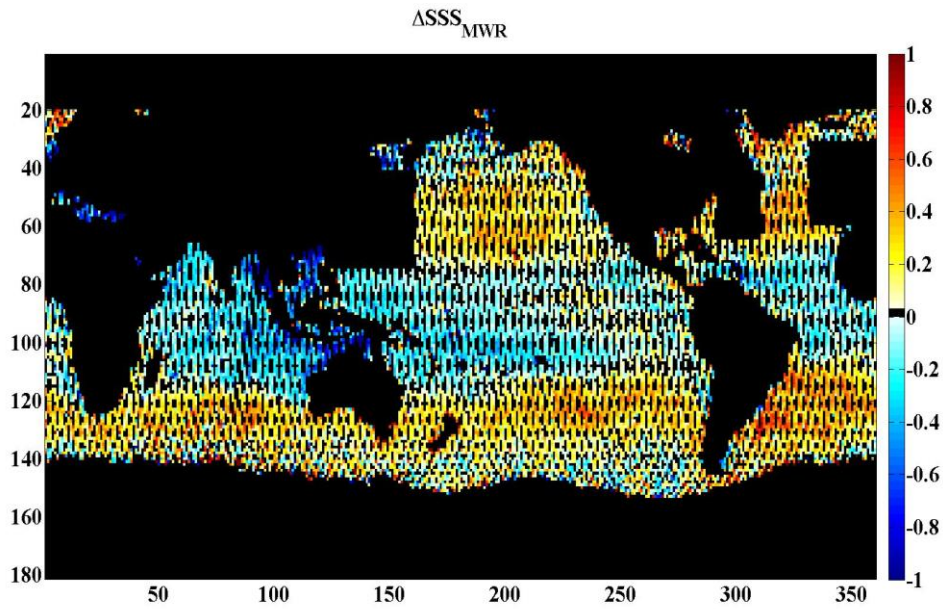


Figure 31 Global delta sea surface salinity derived using MWR roughness correction.

Figure 32 shows two histograms of the global ΔSSS for AQ and MWR for the year of 2013. A Gaussian fit is applied to the global points and the mean and standard deviation of the points are calculated. On a global scale, more than 80% of the points have ΔSSS less than 0.5 psu, and the global mean for both salinity retrievals is 0.06 psu. This represents a high level of agreement with the global HYCOM SSS.

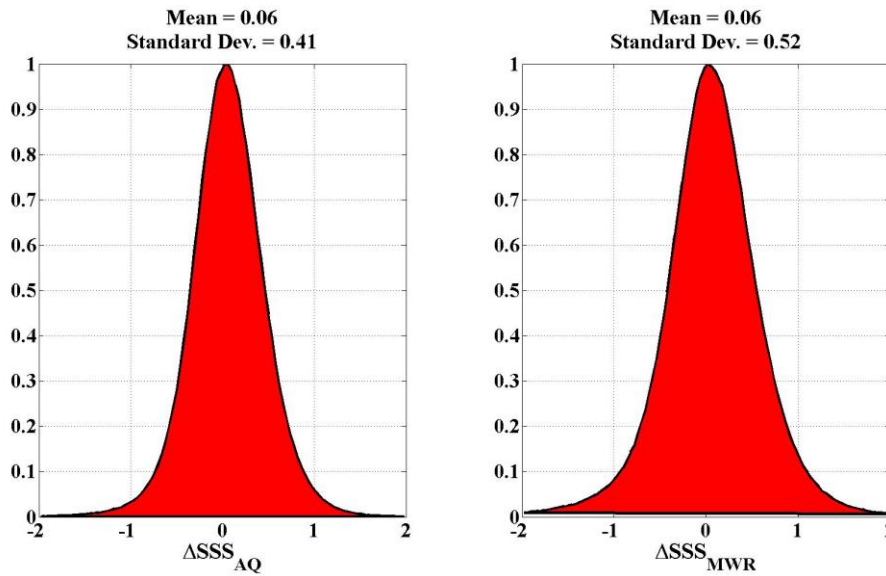


Figure 32 Histograms of global salinity differences.

The double differences between the two salinity retrievals can provide information about the correlation between the two techniques. The double differences can be expressed as,

$$DD = \Delta SSS_{MWR} - \Delta SSS_{AQ} \quad (17)$$

where DD is the double difference.

Figure 33 shows the relationship between the DD and scatterometer wind speed, and between the DD and the relative wind direction. As shown in the figure, there is no systematic correlation between the DD and WS , and DD and WD , which means that the two techniques are statistically independent.

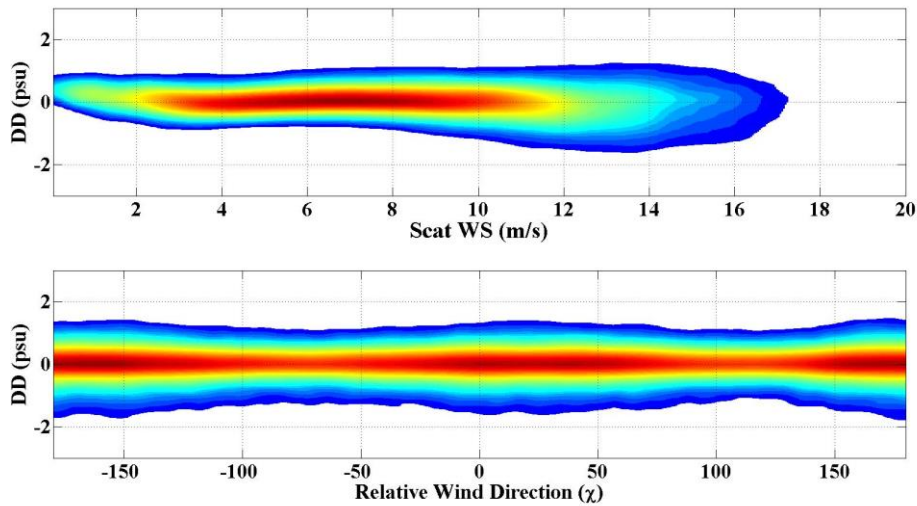


Figure 33 Salinity double differences. Top panel shows the relation between wind speed and the double differences and the bottom panel shows the relation between the relative wind direction and the double differences.

Since both corrections are statistically independent, the combination of both can be significant improvement over either alone and will improve SSS retrievals for wind speeds less or equal to 15 m/s. Further studies will include a combined roughness from the scatterometer and MWR Tb.

CHAPTER 7: SUMMARY

A study was conducted to use the MicroWave Radiometer brightness temperature measurements that are coincident with the Aquarius brightness temperature measurements to provide an alternative ocean roughness correction for the Aquarius sea surface salinity measurements.

An empirical CFRSL ocean surface emissivity RTM was developed, by tuning its coefficients of the model to match on-orbit measurements from both the Aquarius and the MicroWave Radiometer instruments. At first, the specular emissivity was updated using the AQ seawater dielectric model. Next, an iterative technique of varying the emissivity model coefficients was used to reduce the statistical error between the modeled ocean Tb and the measured ocean surface Tb data (L-band and Ka-band), yielding a Radiative Transfer Model that characterizes the ocean surface emissivity and accounts for the wind speed and wind direction effects.

A match-up data set was generated using simultaneous Aquarius and MicroWave Radiometer measurements that are collocated in space and time with ancillary data, numerical weather prediction environmental data, and other microwave instruments geophysical data (WindSat and SSMIS).

The modeled AQ roughness using MWR was compared to the scatterometer-derived roughness baseline present in the AQ Level-2 V3.0 data. While these techniques are independent, the excess roughness correction comparisons were shown to be highly correlated using multi-year observations.

Finally, the quality of the roughness correction was tested in the AQ standard salinity retrieval algorithm. After obtaining the corrected smooth Tb and retrieving SSS, the SSS retrievals were compared to HYCOM_{SSS} to calculate observed differences. Then the salinity differences were analyzed to determine if there was any statistical dependence upon the scatterometer wind speed (included in Level-2). Results indicated that neither AQ SSS retrievals (using the scatterometer) nor the MWR exhibited any systematic dependence on wind speed, which is a proof that both performed equally well.

6.1 Future Work

Unfortunately the MWR stopped providing reliable data after almost three years; so the continued production of MWR roughness correction is not possible. However, there exists an important 3-year MWR legacy data set, which will be processed by CONAE and supplied to the science community. This algorithm will be documented in an Algorithm Theoretical Basis Document (ATBD) and processing code delivered to CONAE to produce this valuable data set.

Also, future work is needed to exploit the combined scat-derived and MWR-derived roughness corrections to provide a statistically improved SSS retrieval. Also, since much of the disagreement between MWR- and Scat-derived roughness correction occurs at high wind speed, it may be possible to improve the MWR forward model and /or the wind direction correction to yield improved results. Increasing the training set to include scat-derived roughness parameters may be use to improve the MWR models.

APPENDIX A
SMOOTH SEA SURFACE EMISSIVITY

Deep within the ocean, the salty water medium behaves as a blackbody and radiates microwave electromagnetic (EM) energy isotropically according to Rayleigh-Jeans law [26] that is expressed as,

$$B_{bb} = \frac{2f^2kT}{c^2} = \frac{2kT}{\lambda^2} \quad (18)$$

where B_{bb} is the blackbody brightness (W/m²/sr/Hz), f is the frequency (Hz), k is Boltzmann's constant (1.38×10⁻²³ J/K), T is the physical temperature of the ocean water (K), c is velocity of light (3×10⁸ m/s) and λ is the wavelength (m).

However, ocean blackbody radiation propagating to the air-sea surface, encounters a dramatic change in the characteristic impedances at this boundary. To illustrate this phenomena, examine the cartoon given in Figure 34, where much of the energy is reflected (and absorbed) internally and only a fraction will pass through the water-air boundary (at a slightly different angle of propagation, θ_2). The efficiency of energy transfer between the interior ocean and the air is called the ocean surface emissivity. This power ratio, defined as the radiation intensity emitted by the surface (B_{gb}) to the total blackbody radiation (B_{bb}), is expressed as,

$$\varepsilon = \frac{B_{gb}}{B_{bb}} = \frac{2kT_b}{\lambda^2} \div \frac{2kT}{\lambda^2} = \frac{T_b}{T} \quad (19)$$

where ε is ocean surface emissivity and T_b is the smooth ocean surface brightness temperature (K).

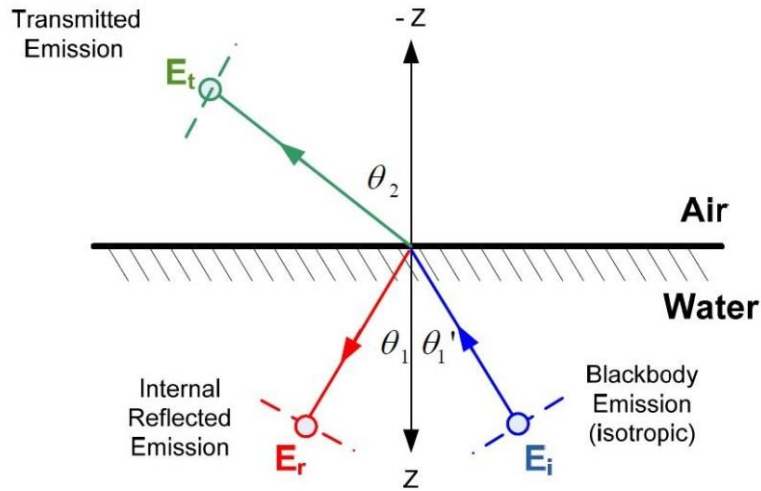


Figure 34 Plane wave electric field reflection and transmission at water-air boundary [10].

Applying the conservation of energy principle, it is clear that the emissivity as a ratio can be expressed as,

$$\varepsilon = 1 - \Gamma \quad (20)$$

where,

Γ = power reflection coefficient = $|\rho|^2$, and ρ = Fresnel voltage reflection coefficient.

The Fresnel voltage reflection coefficient is well known from optics and depends upon the EM direction of propagation and polarization and upon the dielectric properties of the two media (ocean and air). The electric field has two components; one component is perpendicular to the plane of the incidence angle (Horizontal polarization, H-pol), and the other is parallel to the plane

of incidence angle (Vertical polarization, V-pol). The Fresnel voltage reflection coefficient for both polarizations can be expressed as [26],

$$\rho_{V-pol} = - \left[\frac{e_{r2} \cos(\theta) - \sqrt{e_{r2} - \sin^2(\theta)}}{e_{r2} \cos(\theta) + \sqrt{e_{r2} - \sin^2(\theta)}} \right] \quad (21)$$

$$\rho_{H-pol} = \left[\frac{\cos(\theta) - \sqrt{e_{r2} - \sin^2(\theta)}}{\cos(\theta) + \sqrt{e_{r2} - \sin^2(\theta)}} \right] \quad (22)$$

where e_{r2} is the sea water relative complex dielectric constant ($e_{r1} = 1$, for air) and θ is the incidence angle (given as θ_2 in Figure 34).

The key component of the voltage reflection coefficient is the sea water complex dielectric constant, which is a function of the physical temperature and the salt content (salinity) of the water, and the EM frequency. In this dissertation, the complex dielectric model developed for the Aquarius program [32] was adopted.

For this model, the dielectric constant of the water is a complex value with real and imaginary parts, each of which are a function of frequency, sea surface temperature (SST) and salinity (dissolved salt content). These are shown in Figure 23 as a function of frequency for fresh water (salinity = 0 psu [24]) and salt water (salinity = 25, 30, 35 and 40 psu) at a constant SST of 25°C.

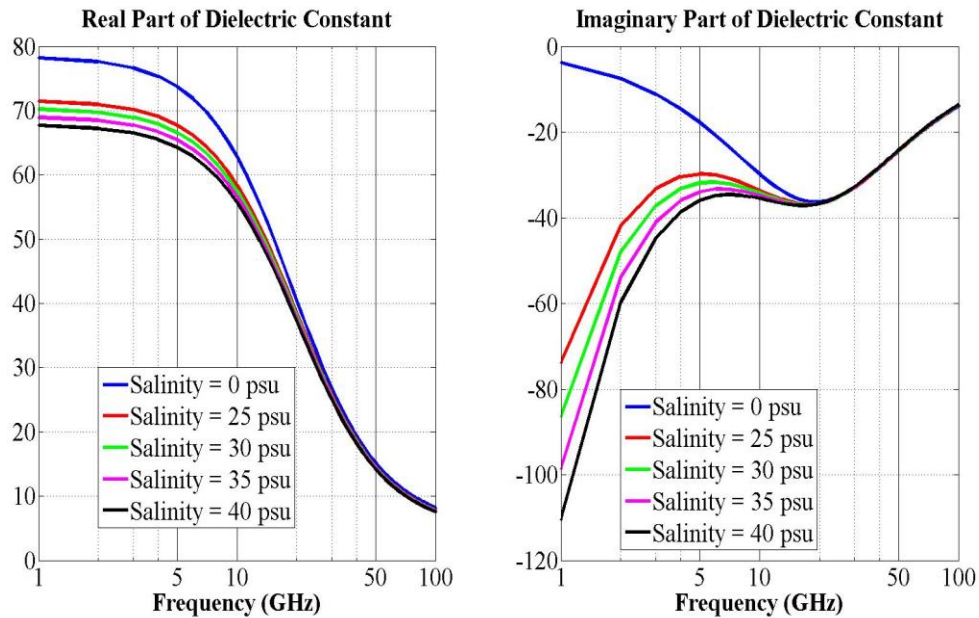


Figure 35 The real part (left panel) and imaginary part (right panel) of the dielectric constant for salinity values of 0, 25, 30, 35 and 40 psu at sea surface temperature of 25 C°.

The smooth ocean power reflection coefficients for V- and H-pol are calculated using the absolute magnitude of the square of the respective Fresnel voltage coefficients using Equations (21) and (22). Results shown in Figure 36 illustrate the earth incidence angle (EIA) dependence of the V-pol and the H-pol reflection coefficients at a constant sea surface temperature (25 C°), salinity (34 psu) and frequency (1.413 GHz). The H-pol and V-pol power reflection coefficients are equal at nadir (EIA = 0°), and as the EIA increases the H-pol reflectivity increases monotonically until it reaches unity at 90°, while the V-pol will decrease and reach its minimum at ~ 83° (Brewster angle, where no internal reflection occurs). After the Brewster angle the reflectivity increases rapidly to unity.

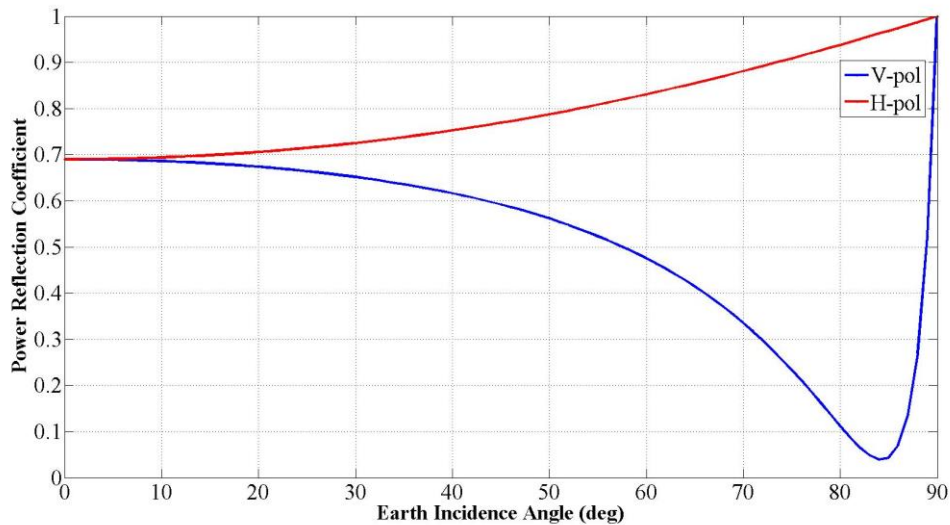


Figure 36 Power reflection coefficient for vertical and horizontal polarizations at constant sea surface temperature (25 C°), salinity (34 psu), at the AQ frequency (1.413 GHz).

Once the reflectivity of sea surface is known, the ocean emissivity can be calculated by applying the conservation of energy principle in Equation (20). The Tb of the ocean (Tb_{ocean}) is the result of multiplication of sea surface emissivity (ϵ_{ocean}) by the physical SST, as follows,

$$Tb_{ocean} = \epsilon_{ocean} \times SST \quad (23)$$

The concept of radiative transfer for a satellite radiometer is illustrated in Figure 37. The total apparent Tb (Tb_{app}) received by a satellite radiometer is the scalar sum of three non-coherent components of Tb at the top of the atmosphere, namely; Tb_{ocean} , atmospheric upwelling Tb (Tb_{up}) and downwelling Tb (Tb_{down}) reflected off of the surface of the ocean (Tb_{ref}). Thus the Tb_{app} is expressed as,

$$Tb_{app} = Tb_{up} + \tau \times (Tb_{ocean} + \tau \times Tb_{down}) \quad (24)$$

where τ is the total (one-way) atmospheric transmissivity.

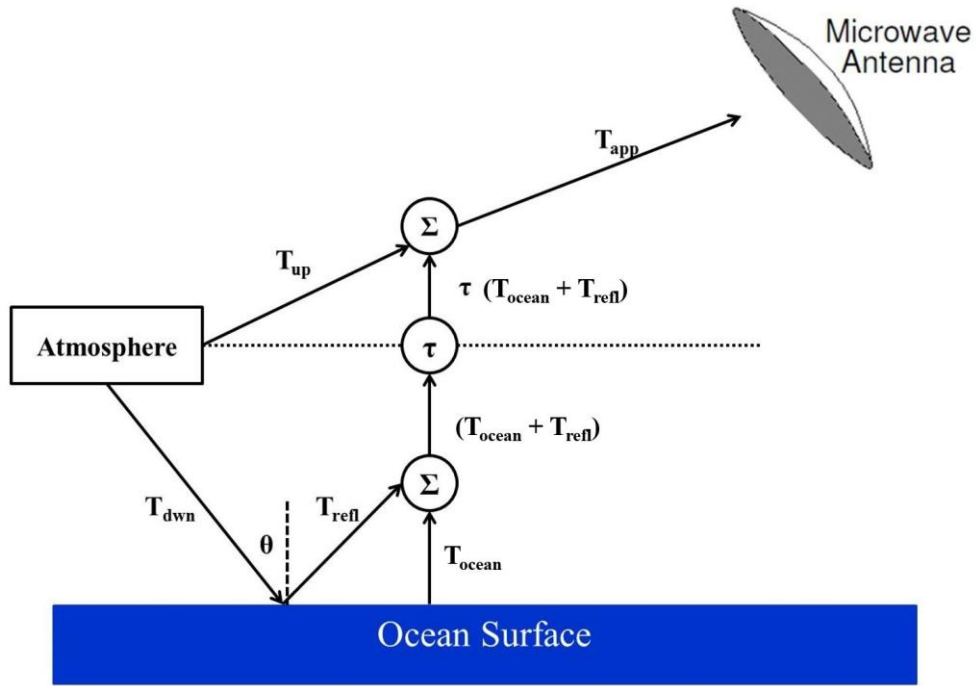


Figure 37 Microwave radiative transfer block-diagram over ocean.

Signal processing and atmospheric corrections need to be applied to the signal received by the microwave antenna to retrieve the signal that is produced by the ocean (T_{ocean}), since it carries information about the ocean surface (sea surface salinity, in this dissertation).

In *Appendix C*, the more detail study is presented about the ocean brightness temperature.

APPENDIX B
SALINITY EFFECTS ON OCEAN EMISSIVITY

At microwave frequencies < 5 GHz, the complex (real and imaginary) dielectric constant of sea water varies significantly with salinity; therefore it is possible (in theory) to retrieve salinity from smooth ocean T_b . However, at these frequencies, the ocean T_b also has a stronger dependence on SST, which mixes these two geophysical signals and complicates the retrievals of each. Fortunately at ~ 1 GHz, there is a very weak dependence of the ocean T_b on SST, which tends to decouple the SST and salinity signals and significantly improves the opportunity to retrieve salinity. On the other hand, the L-band (1-2 GHz) portion of the EM spectrum is heavily populated with active microwave communications and radar systems, which prevent their use for passive microwave sensing, that is with the exception of an important radio astronomy band at $1.413 \text{ GHz} \pm 13 \text{ MHz}$ which is exclusively reserved for passive microwave remote sensing. Thus the choice of the L-band radiometer frequency was dictated by these important factors: i.e., sensitivity to salinity, weakly sensitive to SST and within a protected radio frequency band.

Thus, from a number of airborne radiometer experiments [1], it was demonstrated that the smooth ocean T_b (1.413 GHz) can be used to retrieve the unknown sea surface salinity (SSS) given independent measurements of SST. An example of the calculated smooth surface emissivity of the ocean is given in Figure 38 for SST of 25 C and at two salinity values (10 and 30 psu). Over this large range of salinities, the change of emissivity is only about 5% that results in a sensitivity of $\sim 0.7 \text{ K/psu}$, which is a weak (but measurable) signal.

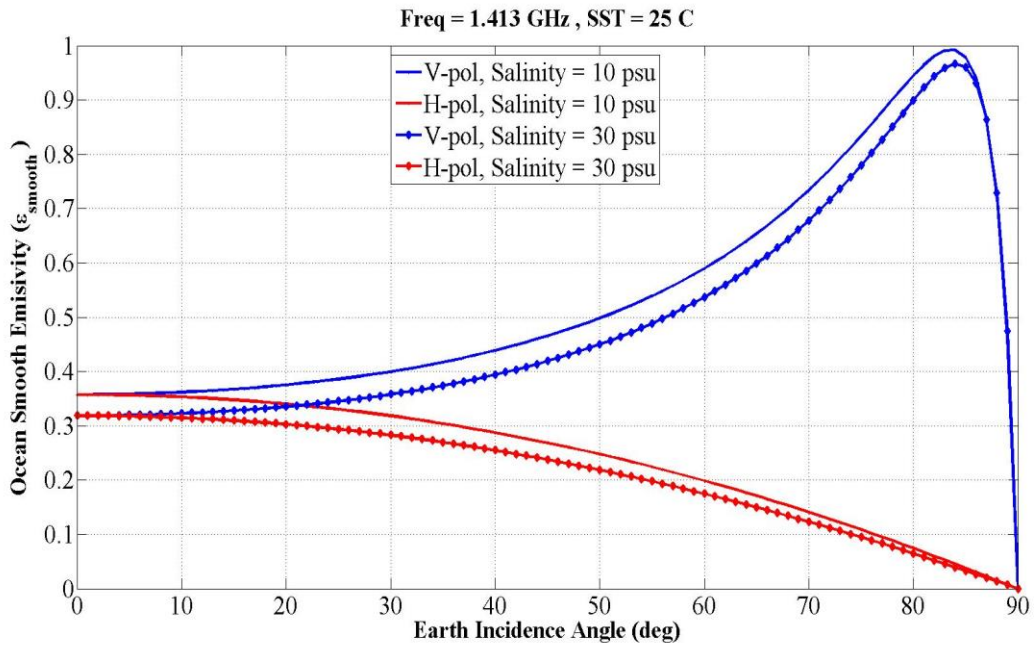


Figure 38 Smooth sea surface emissivity at 1.413 GHz for 25 C° SST, and 10 and 30 psu salinity.

APPENDIX C
ROUGH SEA SURFACE EMISSIVITY

As wind blows over the ocean's surface, capillary waves are formed and non-linear wave-to-wave interactions transfers energy to longer waves, which increases the ocean surface roughness (RMS slope). In turn, this increase in ocean roughness causes a monotonic reduction in the ocean surface reflectivity, which increases the surface emissivity and warms the surface Tb.

In 1967, Stogrin [11] used previous studies ([12]) to model this incremental increase in emissivity as an additive term, thus making the sea surface emissivity (ϵ_{ocean}) a summation of the specular emissivity (ϵ_{smooth}) (based upon the Fresnel power reflection coefficient, detailed description of the smooth surface emissivity id provided in *Appendix A*) and the rough surface emissivity (ϵ_{rough}),

$$\epsilon_{ocean} = \epsilon_{smooth}(freq, SST, SSS, \theta, POL) + \epsilon_{rough}(freq, WS, \chi, \theta, POL) \quad (25)$$

where *freq* is the operating frequency, *POL* is the polarization of the electromagnetic energy (EM) (Vertical or Horizontal), θ is the earth incidence angle (EIA), *WS* is the wind speed (m/s), and χ is the relative wind direction (deg) based upon the EM azimuthal propagation direction.

The existence of surface winds affects the ocean surface emissivity in two ways:

1. Small-scale waves produce an anisotropic roughness that monotonically increases the surface emissivity as a function of the surface friction wind speed [33], and.
2. At surface wind speeds above 6-7 m/s, the breaking ocean gravity waves create a layer of foam floating on the surface of the ocean that further increases the surface emissivity.

Therefore, these two factors will divide the area of the instantaneous field of view (IFOV) to two parts; foam-covered part and non-foam-covered part. Each of these factors will be analyzed separately.

Wind speed and wind direction effect

The ϵ_{rough} term of Equation (25) can be parameterized as a function of frequency, wind speed and relative wind direction (which is defined as the differential azimuth viewing direction of the antenna beam relative to the wind direction [34], *Appendix E*). The wind speed effect ($\epsilon_{rough,ws}$) is an isotropic term and the relative wind direction effect ($\epsilon_{rough,\chi}$) is the anisotropic (zero mean) term, which are additive [18, 35]. That is expressed as follows,

$$\epsilon_{rough_i} = \epsilon_{rough_{WS}}(WS, \theta, freq, SST) + \epsilon_{rough_\chi}(WS, \chi, \theta, freq) \quad (26)$$

where $\epsilon_{rough,ws}$ is the isotropic emissivity of the rough ocean surface, $i = v, h$ denotes the polarization, $freq$ is the EM frequency and χ is the relative wind direction and $\epsilon_{rough,\chi}$ is the anisotropic emissivity of the relative wind direction, and can be expressed as,

$$\epsilon_{rough_\chi} = \beta_{1_i}(WS, \theta, freq) \times \cos(\chi) + \beta_{2_i}(WS, \theta, freq) \times \cos(2\chi) \quad (27)$$

where β_1 and β_2 are the first and the second harmonics coefficients. The first harmonic coefficient (β_1) determines the characteristics of the wind directional signal during up-winds (wind is blowing directly towards the looking angle of the beam, $\chi=0^\circ$) and down-winds (wind is blowing directly away from the looking angle of the beam, $\chi=180^\circ$), and the second harmonic coefficient (β_2) determines the characteristics of the wind directional signal during cross-winds [36].

Sea foam effect

When sea surface waves break, the layer of sea foam that forms decreases the internal reflectivity of the parts of the ocean surface covered by foam, increasing the emissivity of sea water at the water-air boundary, allowing more EM energy to leave the surface. Experiments have shown that emissivity of sea foam depends upon the microwave frequency, polarization, EIA and SST [37, 38]. This increase in emissivity affects only the area of the satellite foot print that is covered with foam, and this percentage of the area of foot print that is covered by foam is referred as Foam Fraction, and it is highly dependent on wind speed; the higher the wind speed gets, more foam will form on the surface due to breaking waves [10]. Monahan [39] characterizes the increase of foam fraction as a function of wind speed and independent of the radiometer parameters: frequency, polarization and EIA.

As a result, the ocean emissivity due to foam (ϵ_{foam}) will equal the multiplication of the sea foam emissivity (a function of frequency, EIA and WS) and foam fraction (FF). It is worth mentioning that the appearance of foam starts at wind speeds equal or higher than 6 m/s.

$$\epsilon_{foam} = FF \times \epsilon_{foam}(freq, \theta, WS) \quad (28)$$

APPENDIX D
CENTRAL FLORIDA REMOTE SENSING LABORATORY
EMISSIVITY MODEL

El-Nimri et al. [10, 40] developed a generalized microwave radiometric ocean surface emissivity model, known hereafter as the CFRSL model, that was tuned using ocean surface T_b measurements from a variety of different airborne and satellite radiometer systems, which operated at a variety of frequencies and earth incidence angles. The basis of his model was a physical ocean emissivity model by Stogryn [11] that calculates ocean emissivity as a function of frequency, EIA and WS. The CFRSL model was primarily developed using measurements at C-band (4-8 GHz) from the National Oceanic and Atmospheric Administration (NOAA) Stepped Frequency Microwave Radiometer (SMFR) [41] and WindSat hurricane observations [42]. The general form of the model is,

$$\epsilon_{ocean\ total} = FF \times \epsilon_{foam}(freq, EIA, WS) + (1 - FF) \times (\epsilon_{smooth} + \epsilon_{rough}) \quad (29)$$

where $\epsilon_{ocean\ total}$ is the total emissivity of the ocean, FF is the foam area coverage fraction, ϵ_{foam} is the emissivity of sea foam, ϵ_{smooth} is the smooth (Fresnel) sea surface emissivity and ϵ_{rough} is the rough sea surface emissivity. Note that all of these parameters (except ϵ_{smooth}) are nonlinear functions of the ocean WS.

CFRSL smooth surface emissivity

The key to measuring the smooth surface emissivity is to know the dielectric behavior of the water at the water-air boundary. The complex dielectric constant is a function frequency and geophysical parameters (sea surface temperature and sea surface salinity).

In the past, several dielectric constant models of sea water have been developed using experimental microwave measurements but the one that was adopted by El-Nimri [10] was developed by Meissner and Wentz [32] for the Aquarius program.

CFRSL foam emissivity

In El-Nimri study [10], several sources of foam emissivity data, at different frequencies and incidences angles, were used to extrapolate existing C-band foam models (Droppleman [38], Stogryn [37] and Rose [43]) to a wider range of frequencies; mainly, L-band and Ka-band (the operating frequencies of Aquarius and MWR). It is worth to mention that the emissivity of foam was independent of the wind speed values at lower frequencies (L-band) and higher frequencies (Ka-band). Further, the foam emissivity only affects foam-covered areas, which are defined by the foam area coverage fraction value. Since FF is dependent only upon wind speed and independent of frequency or EIA, it is valid to be used at different frequency ranges. The foam fraction used in the CFRSL model increases approximately exponentially from $WS = 10$ m/s to 30 m/s as shown in Figure 39

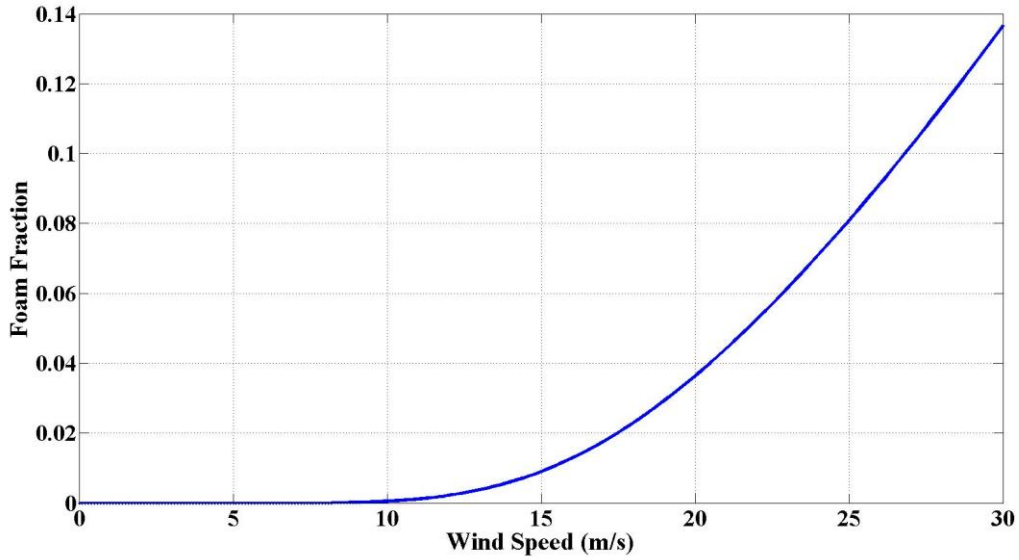


Figure 39 Foam fraction as a function of wind speed.

CFRSL roughness emissivity

For the CFRSL model in Equation (29), the rough ocean emissivity was a function of frequency, polarization, EIA, SST and WS using the relations given below,

For H-pol:

$$\varepsilon_{rough_{WS}}(EIA, WS, freq, SST) = (a_1 \times Z_{EIA} + a_2 \times Z_{WS} + a_3 \times Z_{EIA} \times Z_{WS}) \frac{\sqrt[4]{freq}}{SST} \quad (30)$$

where $Z_{EIA} = 0.5 + \tan^{-1}((EIA - b_1)/b_2)/\pi$, and $Z_{WS} = 0.5 + (\tan^{-1}((WS - c_1)/c_2))/\pi$.

For V-pol:

$$\varepsilon_{rough_{WS}}(EIA, WS, freq, SST) = (a_0 + a_1 \times Z_{EIA} + a_2 \times Z_{WS} + a_3 \times Z_{EIA} \times Z_{WS}) \frac{\sqrt[4]{freq}}{SST} \quad (31)$$

where $Z_{EIA} = \exp(-1 \times \exp((EIA - b_1)/b_2))$, and $Z_{WS} = \exp(-1 \times \exp((WS - c_1)/c_2))$.

The values of a , b and c coefficients are given in Table 8.

Table 8 Coefficients of wind speed effect model.

V-Pol						H-Pol					
Coef	Value	Coef	Value	Coef	Value	Coef	Value	Coef	Value	Coef	Value
a ₀	0.448	b ₁	53.256	c ₁	9.255	--		b ₁	67.074	c ₁	11.850
a ₁	-0.999	b ₂	4.800	c ₂	3.829	a ₁	-14.488	b ₂	29.243	c ₂	10.985
a ₂	3.704	--	--	--	--	a ₂	0.665	--	--	--	--
a ₃	-1.388	--	--	--	--	a ₃	61.279	--	--	--	--

As shown in Equations (30) and (31), the CFRSL model did not account for relative wind direction effects. In Chapter 3, the effects of wind speed and wind direction are explained as well as the CFRSL model tuning process.

APPENDIX E
RELATIVE WIND DIRECTION

The wind direction is the angle between the Earth's north vector and the direction of the wind when measured in clock-wise direction. There are two terminology conventions that describe the wind direction; the first is the *Oceanography Convention* and the second the *Meteorology Convention*. The oceanography convention measures the angle between the north and the vector that points to the direction to which the wind is blowing, while the meteorology convention measures the angle between the north and the vector that points to the direction from which the wind is blowing [44]. Figure 40 shows a cartoon that represents the difference in the measurement of the wind direction relative to north using each of the conventions, and note that there is a 180° shift between the two angles. In this dissertation the oceanography convention is used.

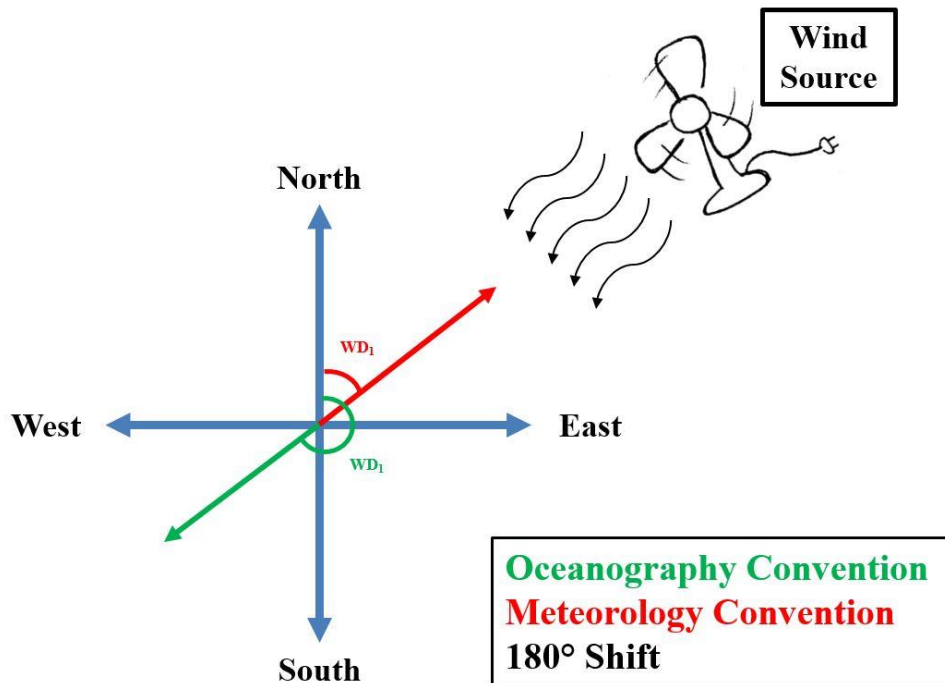


Figure 40 Oceanography and meteorology convention for wind direction measurements

Calculating the relative wind direction requires knowledge of the wind direction angle and the azimuth angle of the antenna line-of-sight. As illustrated in Figure 41, the azimuth “Antenna Look Angle” is the angle measured clockwise relative to the North that points to the center of the antenna IFOV on the earth’s surface. For this measurement the origin of the coordinate system is centered on the sub-satellite point. As the satellite flies in its orbit, the satellite flight direction changes with latitude as does the antenna azimuth angle, but the change is periodic and is repeated every orbit.

Figure 42 shows the azimuth angles of the 8 forward-looking beams (Ka-band beams) of MWR for one orbit. The Aquarius/SAC-D spacecraft starts its orbit at the South Pole, and passes through the equator to the North Pole in the ascending pass, and through the equator and to the South Pole again during the descending pass.

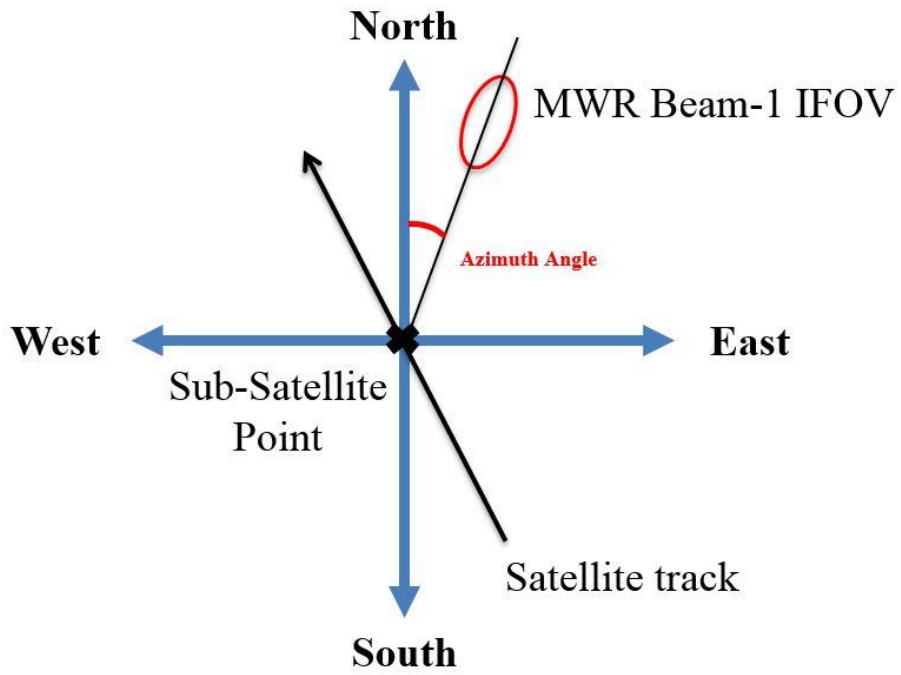


Figure 41 Azimuth angle measurement.

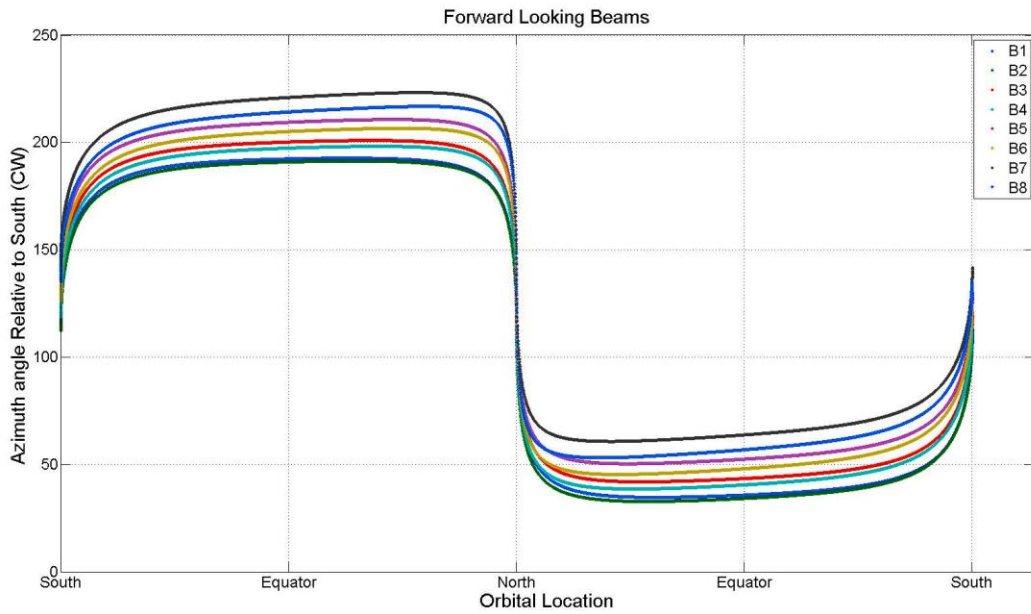


Figure 42 Azimuth angles of the 8 MWR forward looking beams for one orbit

In general, ocean wind direction is highly variable as it changes with weather patterns and time, and it produces an anisotropic variation in the observed ocean surface brightness temperature and radar backscatter [45] that is harmonically related to the *Relative Wind Direction* (denoted by χ). The relative wind direction is defined as differential wind direction relative to the antenna beam line of sight “viewing angle” (azimuth) [34]. Figure 43 [44] shows the relative wind direction values for upwind ($\chi = 0^\circ$, wind is blowing directly towards the antenna), downwind ($\chi = 180^\circ$, wind is blowing directly away from the antenna) and crosswind ($\chi = \pm 90^\circ$, wind is blowing right angles to the antenna viewing angle).

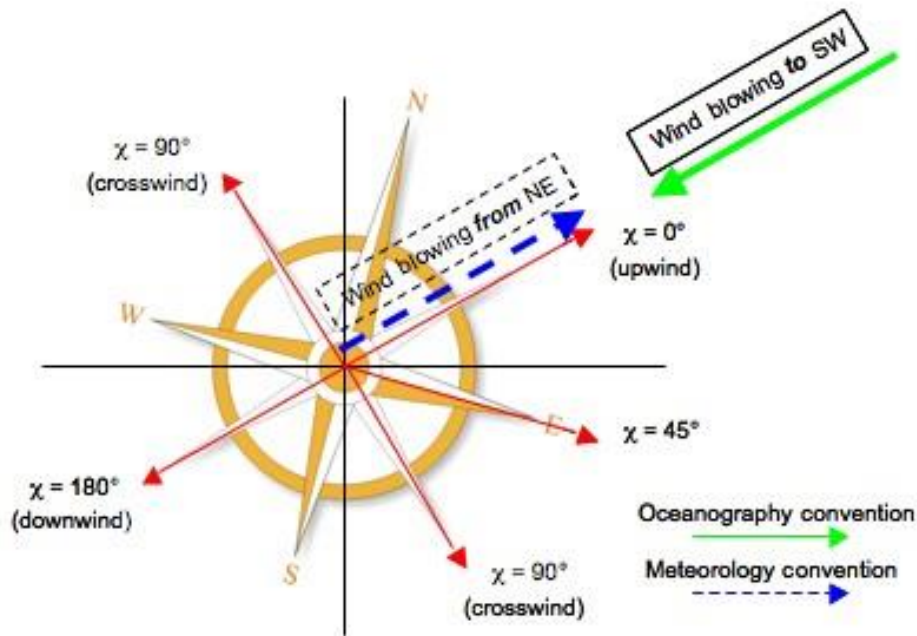


Figure 43 Relative wind direction measurement [44].

The wind direction has an anisotropic effect on the ocean measured surface brightness temperature and can be modeled as,

$$\Delta\varepsilon_{WD} = \beta_1(WS, EIA, freq, POL) \times \cos(\chi) + \beta_2(WS, EIA, freq, POL) \times \cos(2\chi) \quad (32)$$

where WS is the surface wind speed, EIA is the earth incidence angle, $freq$ is the operating frequency, POL is the polarization and χ is the relative wind direction. β_1 and β_2 are the first and second harmonics of the wind direction effect.

The “beta” coefficients can be expressed using an 8th order polynomial, where wind speed is the input,

$$\beta_i = a_7WS^7 + a_6WS^6 + a_5WS^5 + a_4WS^4 + a_3WS^3 + a_2WS^2 + a_1WS + a_0 \quad (33)$$

where $i=1$ or 2 denoting the first and second harmonics coefficients.

The a coefficients for β_1 and β_2 are tabulated in Table 9 based upon frequency, polarization and EIA.

Table 9 The coefficients of the 8th order polynomial for the first and the second harmonics of the wind direction effects for all frequency, polarization and incidence angle values.

Beam	β_1							
	a7	a6	a5	a4	a3	a2	a1	a0
Ka V-pol Odd	0.000000700	-0.0000051492	0.0001369777	-0.0017667730	0.0108639663	-0.0251061818	0.0405021178	-0.0206604578
Ka V-pol Even	0.0000001742	-0.0000129521	0.0003781664	-0.0054441722	0.0394833451	-0.1305894405	0.1814320536	-0.0339554925
Ka H-pol Odd	0.0000004372	-0.0000318810	0.0009042478	-0.0124459333	0.0837695059	-0.2421359447	0.2530496893	-0.0461193113
Ka H-pol Even	0.0000002240	-0.0000161655	0.0004571636	-0.0062235869	0.0393269564	-0.0859160706	0.0400050718	-0.0155083522
L V-pol Beam 1	0.0000000245	-0.0000013633	0.0000224415	-0.0000590000	-0.0011732103	0.0073429597	-0.0033175709	-0.0061699580
L V-pol Beam 2	0.0000000000	0.0000000000	-0.0000000700	0.0000406684	-0.0006256075	0.0052449896	-0.0077358535	-0.0030828662
L V-pol Beam 3	0.0000000485	-0.0000035501	0.0001002599	-0.0013895978	0.0098898572	-0.0320680626	0.0397131500	-0.0156091316
L H-pol Beam 1	0.0000000000	0.0000000111	0.0000016162	-0.0001176355	0.0024017127	-0.0177636384	0.0446800218	-0.0410394872
L H-pol Beam 2	-0.0000000530	0.0000046992	-0.0001522841	0.0024413530	-0.0202202600	0.0821274075	-0.1262668625	-0.0034351374
L H-pol Beam 3	0.0000000084	-0.0000004983	0.0000107261	-0.0000940000	0.0000704711	0.0055184857	-0.0252733998	-0.0158703342
Beam	β_2							
	a7	a6	a5	a4	a3	a2	a1	a0
Ka V-pol Odd	-0.0000003010	0.0000217975	-0.0005934849	0.0078892934	-0.0528165444	0.1665475820	-0.1998477733	0.0315391061
Ka V-pol Even	0.0000003202	-0.0000230000	0.0006552795	-0.0091758538	0.0662192005	-0.2274012408	0.2752325103	-0.0396793679
Ka H-pol Odd	-0.0000001947	0.0000168971	-0.0005609450	0.0088722047	-0.0675961022	0.2239662076	-0.2704559723	0.0612410421
Ka H-pol Even	-0.0000004405	0.0000382542	-0.0012798644	0.0208504487	-0.1708706124	0.6529863642	-0.9134373087	0.0693976274
L V-pol Beam 1	0.0000000409	-0.0000025447	0.0000556580	-0.0005559298	0.0036894237	-0.0195922935	0.0396106024	0.0170504521
L V-pol Beam 2	0.0000000811	-0.0000060794	0.0001774198	-0.0026110547	0.0209814849	-0.0863290846	0.1283543787	0.0208273294
L V-pol Beam 3	0.0000000100	-0.0000011438	0.0000480460	-0.0010209927	0.0118713646	-0.0672854236	0.1254040342	0.0283057115
L H-pol Beam 1	0.0000000000	0.0000000000	-0.0000039000	0.0001745750	-0.0021272231	0.0068696823	0.0065355783	-0.0314713597
L H-pol Beam 2	-0.0000001216	0.0000099635	-0.0003216032	0.0051601906	-0.0423984298	0.1638989294	-0.2291388029	0.0275472409
L H-pol Beam 3	0.0000000000	0.0000001082	-0.0000100353	0.0002955614	-0.0034638559	0.0156012007	-0.0212927450	0.0047598250

APPENDIX F
AQUARIUS SCATTEROMETER ROUGHNESS CORRECTION

The Level-2 Version 3.0 Aquarius data product, uses the scatterometer-derived wind speeds, NCEP wind speed and wind direction, significant wave height (SWH) information (provided by the National Oceanic and Atmospheric Administration, NOAA), Reynold SST and the radiometer measurements to provide a surface roughness correction [46]. The Aquarius roughness can be expressed as,

$$\Delta\epsilon_{rough} = \Delta\epsilon_{WS_0}(WS, \chi, SST) + \Delta\epsilon_{WS_1}(WS, \sigma_{0,VV}) + \Delta\epsilon_{WS_2}(WS, SWH) \quad (34)$$

where $\Delta\epsilon_{rough}$ is the surface ocean roughness and it comprises three additive terms; the first ($\Delta\epsilon_{WS_0}$) which is a function of scatterometer wind speed (WS) and sea surface temperature (SST), the second ($\Delta\epsilon_{WS_1}$) which is a function of scatterometer wind speed and vertical scatterometer backscatter ($\sigma_{0,VV}$) and the third ($\Delta\epsilon_{WS_2}$) which is a function of scatterometer wind speed and significant wave height (SWH).

Figure 44 shows the relationship between the radar backscatter and the ocean roughness as wind speed increases. The relationship starts as a monotonically increasing function, then the radar back scatter starts to lose sensitivity to higher wind speeds and starts to saturate.

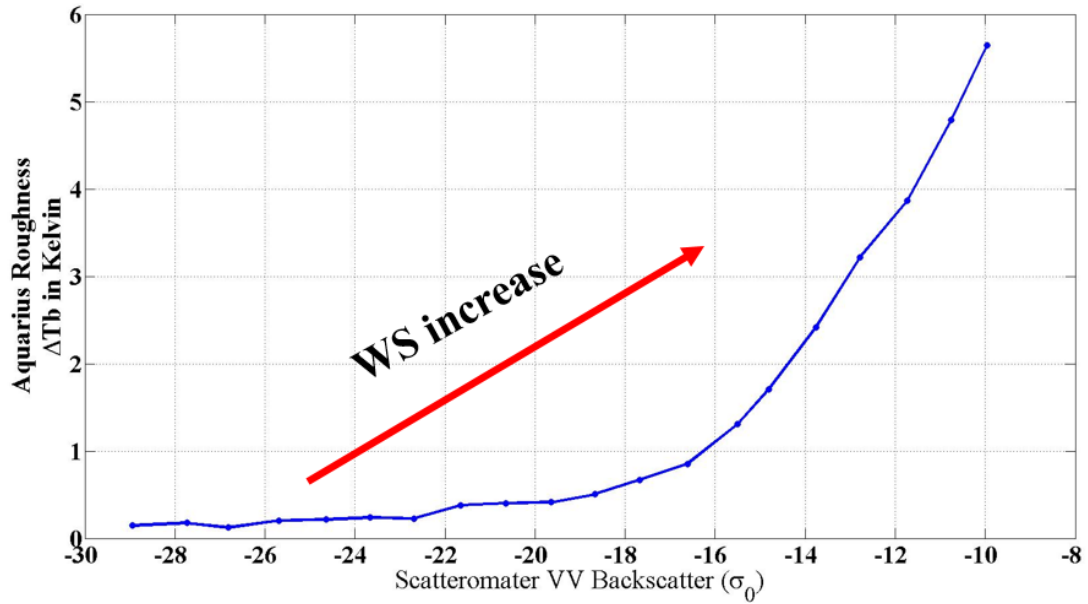


Figure 44 The relationship between the scatterometer vertical backscatter (in dB) and the vertical ocean roughness (in Kelvin).

Figure 45 shows the relationship between the significant wave height, which is directly related to wind speed, and the V-pol ocean roughness.

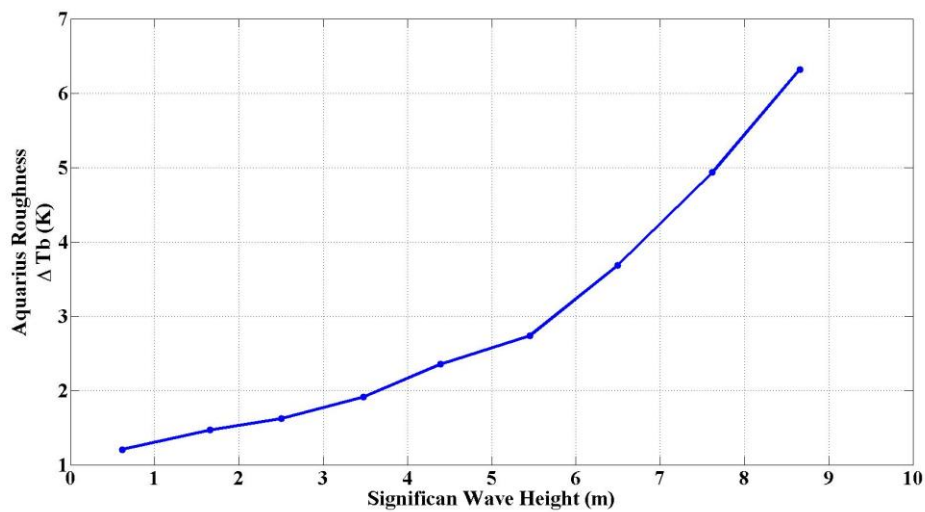


Figure 45 The relationship between the significant wave height (in meters) and the vertical ocean roughness (in Kelvin).

By finding the correlation between those parameters and the measured ocean surface Tb, the AQ team generate a relationship that calculates the ocean roughness correction.

REFERENCES

- [1] D. Le Vine, M. Kao, R. Garvine, and T. Sanders, "Remote sensing of ocean salinity: Results from the Delaware coastal current experiment," *Journal of Atmospheric and Oceanic Technology*, vol. 15, pp. 1478-1484, 1998.
- [2] G. Lagerloef, F. R. Colomb, D. Le Vine, F. Wentz, S. Yueh, C. Ruf, *et al.*, "The Aquarius/SAC-D mission: Designed to meet the salinity remote sensing challenge " *OCEANOGRAPHY*, vol. 21, pp. 68-81, 2008.
- [3] A. Buis, P. Lynch, G. Cook-Anderson, and R. Sullivant, "Aquarius/SAC-D: Studying Earth's salty seas from space," ed: Jun, 2011.
- [4] D. M. Le Vine, G. S. E. Lagerloef, F. R. Colomb, S. H. Yueh, and F. A. Pellerano, "Aquarius: An Instrument to Monitor Sea Surface Salinity From Space," *Geoscience and Remote Sensing, IEEE Transactions on*, vol. 45, pp. 2040-2050, 2007.
- [5] D. M. Le Vine, G. S. E. Lagerloef, F. Pellerano, and F. R. Colomb, "The Aquarius/SAC-D mission and status of the Aquarius instrument," in *Microwave Radiometry and Remote Sensing of the Environment, 2008. MICRORAD 2008*, 2008, pp. 1-4.
- [6] F. A. Pellerano, J. Piepmeier, M. Triesky, K. Horgan, J. Forgiione, J. Caldwell, *et al.*, "The Aquarius Ocean Salinity Mission High Stability L-band Radiometer," in *Geoscience and Remote Sensing Symposium, 2006. IGARSS 2006. IEEE International Conference on*, 2006, pp. 1681-1684.
- [7] D. M. Le Vine, G. S. E. Lagerloef, and S. E. Torrusio, "Aquarius and Remote Sensing of Sea Surface Salinity from Space," *Proceedings of the IEEE*, vol. 98, pp. 688-703, 2010.
- [8] *National Snow & Ice Data Center (NSIDC)*. Available: <http://nsidc.org/data/docs/daac/aquarius/aq2-sm/index.html>
- [9] S. S. Khan, "Simulation of Brightness Temperatures for the MicroWave Radiometer on the Aquarius/SAC-D Mission," Master of Science, Electrical Engineering, University of Central Florida, 2009.
- [10] S. F. El-Nimri, "Development of an Improved Microwave Ocean Surface Emissivity Radiative Transfer Model," Ph.D., Electrical Engineering, University of Central Florida, 2010.
- [11] A. Stogryn, "The apparent temperature of the sea at microwave frequencies," *Antennas and Propagation, IEEE Transactions on*, vol. 15, pp. 278-286, 1967.
- [12] C. Cox and W. Munk, "Measurement of the Roughness of the Sea Surface from Photographs of the Sun's Glitter," *Journal of the Optical Society of America*, vol. 44, pp. 838-850, 1954/11/01 1954.

- [13] T. Meissner and F. J. Wentz, "The Emissivity of the Ocean Surface Between 6 and 90 GHz Over a Large Range of Wind Speeds and Earth Incidence Angles," *Geoscience and Remote Sensing, IEEE Transactions on*, vol. 50, pp. 3004-3026, 2012.
- [14] "Aquarius User Guide," Jet Propulsion Laboratory, Pasadena, California 91109-8099 June 2, 2014.
- [15] *Aquarius: Sea Surface Salinity from Space*. Available: <http://aquarius.umaine.edu/cgi/data.htm>
- [16] S. H. Yueh and J. Chaubell, "Sea Surface Salinity and Wind Retrieval Using Combined Passive and Active L-Band Microwave Observations," *Geoscience and Remote Sensing, IEEE Transactions on*, vol. 50, pp. 1022-1032, 2012.
- [17] S. Yueh, A. Fore, A. Freedman, M. J. Chaubell, W. Tang, and G. Neumann, "Aquarius Scatterometer Algorithm Theoretical Basis Document," March 2012.
- [18] S. H. Yueh, T. Wenqing, A. G. Fore, G. Neumann, A. Hayashi, A. Freedman, *et al.*, "L-Band Passive and Active Microwave Geophysical Model Functions of Ocean Surface Winds and Applications to Aquarius Retrieval," *Geoscience and Remote Sensing, IEEE Transactions on*, vol. 51, pp. 4619-4632, 2013.
- [19] *Remote Sensing Systems Geophysical Retrievals*. Available: <http://www.remss.com/>
- [20] Y. Hejazin, W. L. Jones, and S. El-Nimri, "A roughness correction algorithm for aquarius using MWR," in *Microwave Radiometry and Remote Sensing of the Environment (MicroRad), 2014 13th Specialist Meeting on*, 2014, pp. 44-48.
- [21] S. K. Biswas, S. Farrar, K. Gopalan, A. Santos-Garcia, W. L. Jones, and S. Bilanow, "Intercalibration of Microwave Radiometer Brightness Temperatures for the Global Precipitation Measurement Mission," *Geoscience and Remote Sensing, IEEE Transactions on*, vol. 51, pp. 1465-1477, 2013.
- [22] F. J. Wentz, "Measurement of oceanic wind vector using satellite microwave radiometers," *Geoscience and Remote Sensing, IEEE Transactions on*, vol. 30, pp. 960-972, 1992.
- [23] R. W. Schmitt and Ocean Observing System Development Panel., *The ocean freshwater cycle*. College Station, Tex.: Texas A & M University, 1994.
- [24] E. Lewis, "The practical salinity scale 1978 and its antecedents," *Oceanic Engineering, IEEE Journal of*, vol. 5, pp. 3-8, 1980.
- [25] F. J. Wentz and D. M. Le Vine, "Aquarius Salinity Retrieval Algorithm," August 29, 2012.
- [26] F. T. Ulaby, R. K. Moore, and A. K. Fung, *Microwave remote sensing : active and passive*. Reading, Mass.: Addison-Wesley Pub. Co., Advanced Book Program/World Science Division, 1981.

- [27] T. Meissner, F. Wentz, D. LeVine, and J. Scott, "Aquarius Salinity Retrieval Algorithm," June, 2014.
- [28] *Jet Propulsion Laboratory (JPL) Physical Oceanography Distributed Active Archive Center (PODAAC)*. Available: <http://podaac.jpl.nasa.gov/aquarius>
- [29] E. P. Chassignet, H. E. Hurlburt, O. M. Smedstad, G. R. Halliwell, P. J. Hogan, A. J. Wallcraft, *et al.*, "The HYCOM (HYbrid Coordinate Ocean Model) data assimilative system," *Journal of Marine Systems*, vol. 65, pp. 60-83, 3// 2007.
- [30] A. Santos-Garcia, M. M. Jacob, W. L. Jones, W. E. Asher, Y. Hejazin, H. Ebrahimi, *et al.*, "Investigation of rain effects on Aquarius Sea Surface Salinity measurements," *Journal of Geophysical Research: Oceans*, vol. 119, pp. 7605-7624, 2014.
- [31] *Hybrid Coordinate Ocean Model (HYCOM)*. Available: <http://hycom.org/>
- [32] T. Meissner and F. J. Wentz, "The complex dielectric constant of pure and sea water from microwave satellite observations," *Geoscience and Remote Sensing, IEEE Transactions on*, vol. 42, pp. 1836-1849, 2004.
- [33] F. J. Wentz, "A two-scale scattering model for foam-free sea microwave brightness temperatures," *Journal of Geophysical Research*, vol. 80, pp. 3441-3446, 1975.
- [34] W. Jones, L. C. Schroeder, and J. Mitchell, "Aircraft measurements of the microwave scattering signature of the ocean," *Antennas and Propagation, IEEE Transactions on*, vol. 25, pp. 52-61, 1977.
- [35] N. Tran, D. Vandemark, C. S. Ruf, and B. Chapron, "The dependence of nadir ocean surface emissivity on wind vector as measured with microwave radiometer," *Geoscience and Remote Sensing, IEEE Transactions on*, vol. 40, pp. 515-523, 2002.
- [36] T. Meissner and F. Wentz, "An updated analysis of the ocean surface wind direction signal in passive microwave brightness temperatures," *Geoscience and Remote Sensing, IEEE Transactions on*, vol. 40, pp. 1230-1240, 2002.
- [37] A. Stogryn, "The emissivity of sea foam at microwave frequencies," *Journal of Geophysical Research*, vol. 77, pp. 1658-1666, 1972.
- [38] J. D. Droppleman, "Apparent microwave emissivity of sea foam," *Journal of Geophysical Research*, vol. 75, pp. 696-698, 1970.
- [39] E. C. Monahan and D. K. Woolf, "Comments on "Variations of Whitecap Coverage with Wind stress and Water Temperature," *Journal of Physical Oceanography*, vol. 19, pp. 706-709, 1989/05/01 1989.
- [40] S. F. El-Nimri, W. L. Jones, E. Uhlhorn, C. Ruf, J. Johnson, and P. Black, "An Improved C-Band Ocean Surface Emissivity Model at Hurricane-Force Wind Speeds Over a Wide Range of Earth Incidence Angles," *Geoscience and Remote Sensing Letters, IEEE*, vol. 7, pp. 641-645, 2010.

- [41] E. W. Uhlhorn, P. G. Black, J. L. Franklin, M. Goodberlet, J. Carswell, and A. S. Goldstein, "Hurricane Surface Wind Measurements from an Operational Stepped Frequency Microwave Radiometer," *Monthly Weather Review*, vol. 135, pp. 3070-3085, 2007/09/01 2007.
- [42] C. S. Ruf, "The dependence of the microwave emissivity of the ocean on hurricane force wind speed," in *Proc. 28th Conf. Hurricanes Trop. Meteorol*, 2008.
- [43] L. A. Rose, W. E. Asher, S. C. Reising, P. W. Gaiser, K. M. St Germain, D. J. Dowgiallo, *et al.*, "Radiometric measurements of the microwave emissivity of foam," *Geoscience and Remote Sensing, IEEE Transactions on*, vol. 40, pp. 2619-2625, 2002.
- [44] S. Soisuvann, "An Ocean Surface Wind Vector Model Function For A Spaceborne Microwave Radiometer And Its Application " Ph.D., Electrical Engineering, University of Central Florida, 2006.
- [45] S. H. Yueh, R. Kwok, and S. V. Nghiem, "Polarimetric scattering and emission properties of targets with reflection symmetry," *Radio Science*, vol. 29, pp. 1409-1420, 1994.
- [46] F. W. T. Meissner, D. LeVine, J. Scott, "Addendum III to Aquarius Algrithm Theoretical Basis Document," June 4, 2014 2014.